

An HLLC Riemann Solver for Resistive Relativistic Magnetohydrodynamics

S. Miranda-Aranguren¹*, M.A. Aloy¹†, T. Rembiasz¹

¹Departamento de Astronomía y Astrofísica, Universitat de València, C/. Dr. Moliner 50, 46100 Burjassot, Spain

Accepted XX 2018. Received XX 2017; in original form XX 2018

ABSTRACT

We present a new approximate Riemann solver for the augmented system of equations of resistive relativistic magnetohydrodynamics (RRMHD) that belongs to the family of Harten-Lax-van Leer contact wave (HLLC) solvers. In HLLC solvers, the solution is approximated by two constant states flanked by two shocks separated by a contact wave. The accuracy of the new approximate solver is calibrated through one- and two-dimensional test problems.

Key words: (magnetohydrodynamics) MHD - methods: numerical - relativistic processes - shock waves

1 INTRODUCTION

Relativistic magnetised plasma is ubiquitously found among the most violent and catastrophic phenomena of the Universe. Active galactic nuclei (AGN) (Blandford 2002), Gamma-ray bursts (GRBs; Lyutikov & Blandford 2003), microquasars (Meier 2003; McKinney & Gammie 2004), pulsars and magnetars (Bucciantini et al. 2005; Obergaulinger & Aloy 2017), compact X-ray binaries (Varnière et al. 2002), mergers of binary neutron stars (Rezzolla et al. 2011; Fernández & Metzger 2016) or black holes (Marrone et al. 2007; Palenzuela et al. 2010; Martí-Vidal et al. 2015), etc., may quite generically be endowed with dynamically relevant magnetic fields. From the dynamical point of view, magnetic fields play a main role in the angular momentum transport required for driving accretion in Keplerian discs girding compact objects. The magnetorotational instability (MRI; Velikhov 1959; Chandrasekhar 1960) is likely to be the main mechanism inducing the angular momentum redistribution in accretion discs (e.g., Balbus & Hawley 1991, 1998). Another context where the MRI seems to be crucial for the magnetic field to reach dynamically relevant strength is stellar core collapse. The post-collapsed core of a massive star develops suitable conditions for the magnetic field to be amplified by the MRI (e.g., Akiyama et al. 2003; Obergaulinger et al. 2006; Cerdá-Durán et al. 2007; Sawai et al. 2013; Mösta et al. 2015; Sawai & Yamada 2016). In any of these scenarios, the foremost question is not whether MRI may develop, but instead, which is the primarily mechanism quenching the magnetic field growth before it exhausts all the available

free energy (namely, differential rotational energy) in the system. Compressibility caused by the magnetic field or parasitic instabilities, which can be strongly affected or even triggered by non-ideal effects such as resistivity and viscosity (Goodman & Xu 1994; Latter et al. 2009; Pessah 2010), are commonly invoked as the main agents setting the termination level of the field growth. In the last decade, the basic analytic models for magnetic field saturation have been probed by means of numerical simulations in different physical regimes including viscosity and resistivity (e.g., Rembiasz et al. 2016a,b; Guilet & Müller 2015; Guilet et al. 2015), though none of them has treated the problem of the MRI saturation including relativistic effects.

Relativistic jets generated from compact objects are another example where resistive effects may be instrumental to understanding their generation. In one of the most accepted models of jet formation, magnetic field taps a fraction of the rotational energy of a Kerr black hole (BH) and launches a relativistic beam of very magnetised plasma (e.g. Blandford & Znajek 1977; Beskin & Kuznetsova 2000; Komissarov 2004; Okamoto 2006; McKinney 2006; Tchekhovskoy et al. 2010; Penna et al. 2013). The global structure of the magnetosphere surrounding either a neutron star (NS) or a BH is reasonably well represented assuming that it is force-free. However, it is unlikely that the force-free conditions hold everywhere. For instance, in the case of NSs, there may exist small regions (gaps) where particles are accelerated by the electric field along the magnetic field lines. These processes may explain the magnetospheric emission (Beloborodov & Thompson 2007; Beloborodov 2013b,a; Levinson & Segev 2017). In the case of BH magnetospheres, it is not uncommon that even the simplest topologies of the magnetic field encompass low latitude regions where current-sheets

* sergio.miranda@uv.es
† miguel.a.aloy@uv.es

(which are known to be unstable against the tearing mode (TM) instability; [Furth et al. 1963](#)) are present in the initially computed magnetospheric topologies (e.g., in split-monopole configurations, [Blandford & Znajek 1977](#); [Ghosh 2000](#); [Contopoulos et al. 2013](#); [Nathanail & Contopoulos 2014](#)). They may also develop in the course of the dynamical evolution either arising from the accretion disk ([Goodman & Uzdensky 2008](#); [Parfrey et al. 2015](#)) or due to MHD instabilities of a Poynting-flux dominated flow ([Eichler 1993](#); [Begelman 1998](#); [Giannios & Spruit 2006](#); [Bromberg & Tchekhovskoy 2016](#)).

Beyond the undeniable dynamical influence that non-ideal resistive effects may have on astrophysical sources associated to relativistic outflows, the emission properties of such sources are likely bound to the mechanisms of magnetic field dissipation if the outflows are Poynting-flux dominated ([Thompson 1994](#); [Spruit et al. 2001](#); [Giannios & Spruit 2005](#); [Zhang & Yan 2011](#)). The “internal shocks” or “shock-in-jet” model (e.g., [Rees 1978](#); [Rees & Mészáros 1994](#); [Marscher & Gear 1985](#); [Spada et al. 2001](#); [Bicknell & Wagner 2002](#); [Mimica et al. 2004](#)) has an important role in the understanding of the blazar spectra and has been very often invoked for explaining many of the features of the blazar variability and flares, as well as the prompt emission of GRBs. For the latter, however, there have been claims that the radiation efficiency is too low ([Kumar 1999](#); [Panaiteescu et al. 1999](#); [Kumar & Narayan 2009](#)), though more detailed numerical models seem to ameliorate this potential drawback ([Mimica et al. 2005](#)). Indeed, internal shocks happening in a moderately magnetised plasma can be (much) more efficient converting kinetic energy into thermal *and* magnetic energy than purely hydrodynamic internal collisions ([Mimica et al. 2007](#); [Mimica & Aloy 2010](#)). There are, however, indications that the dissipation of magnetic fields may naturally explain the observed phenomenology as we discuss in the next paragraphs.

First, employing particle-in-cell (PIC) simulations, [Sironi et al. \(2015\)](#) show that magnetic reconnection may deposit more than 50% of the dissipated energy into non-thermal leptons when the magnetic field energy density is larger than the rest-mass energy density. The shock downstream emitting region shows a rough equipartition between magnetic field and radiating particles, accounting naturally for this commonly observed property in blazars. Along the same line, [Petropoulou et al. \(2016\)](#) also conclude that blazar flares naturally result from magnetic reconnection in a magnetically dominated jet.

Second, the lack of a thermal component in the spectrum of some well observed Fermi GRBs (e.g., in GRB 080916C; [Zhang & Pe'er 2009](#)) is taken as an indication of the magnetisation of the radiating plasma flow. The photospheric thermal component, which is expected to appear in the standard “fireball” model, can be much dimmer (unobservable in practice) if the outflow is Poynting dominated ([Zhang & Mészáros 2002](#); [Daigne & Mochkovitch 2002](#)), unless the Poynting flux is directly converted into kinetic energy of the flow below the photosphere (e.g., [Vlahakis & Königl 2003](#)). This means that magnetic dissipation should play a fundamental role shaping the observed spectra.

Third, the short time-scales displayed by the high-

energy emission of either GRBs or blazar jets in AGNs have driven the development of various models where the reconnection of the magnetic field is of paramount importance. Among them, we find the “minijets” or “jets-in-a-jet” model (e.g., [Giannios et al. 2009, 2010](#); [Nalewajko et al. 2011](#); [Giannios 2013](#); [Barniol Duran et al. 2016](#)) and the “fundamental emitters” or “relativistic turbulence” model (e.g., [Blandford 2002](#); [Lyutikov & Blandford 2003](#); [Lyutikov 2006](#); [Kumar & Narayan 2009](#); [Lazar et al. 2009](#); [Narayan & Kumar 2009](#); [Narayan & Piran 2012](#); [O’Riordan et al. 2017](#)). The “jets-in-a-jet” model attributes the TeV emission in relativistic AGN jets to blobs of plasma (plasmoids) where the magnetic field dissipates by reconnection ([Giannios et al. 2009, 2010](#)). Under certain conditions, the reconnection outflows are moderately relativistic and may efficiently power the observed TeV flares through synchrotron-self-Compton emission. The emission of the outflows generated by episodic reconnection events is Doppler boosted by the relativistic jet beam. The resulting TeV flares timescales may be as short as minutes in the context of AGN jets, consistent with that observed in, e.g., M87 ([Aharonian et al. 2006](#); [Acciari et al. 2008](#); [Albert et al. 2008](#)) as well as in the blazars MrK 501 and PKS 2155-304 ([Aharonian et al. 2007](#); [Albert et al. 2007](#)). We note, however, that [Narayan & Piran \(2012\)](#) find that the emission properties (variability) of relativistic turbulent motions in a beam with a sufficiently fast jet (with a Lorentz factor $W > 25$) accommodate more easily the TeV light-curve of the blazar PKS 2155-304 than the standard minijets model.

Fourth, models based upon the reconnection of the magnetic field have also become popular to explain the prompt emission of GRBs. For instance, the *Internal Collision-induced Magnetic Reconnection and Turbulence* (ICMART) model ([Zhang & Yan 2011](#); [Deng et al. 2015](#)) assumes that in an intermittent magnetically dominated outflow ($1 \lesssim \sigma_m \lesssim 100^1$), internal collisions take place. Due to the larger magnetisation of the flow, the first generation of (weak) internal shocks happening at relatively small distances from the central GRB engine ($\sim 10^{13} - 10^{14}$ cm) distort any large scale magnetic field existing in the flow. The successive generations of shell collisions, which take place at distance scales $\sim 10^{15} - 10^{16}$ cm, trigger fast turbulent reconnection (an ICMART event) that may be observed as a broad pulse in the GRB light curve.

Fifth, for typical long GRB jets, [McKinney & Uzdensky \(2012\)](#) find that magnetic reconnection may be avoided due to the high collisional rate of the plasma deep inside the GRB stellar progenitor, until a “reconnection switch” mechanism proceeds catastrophically near the jet photosphere, where radiation is efficiently released.

Many relevant astrophysical phenomena involve shock waves. In the specific context of this paper, the fast magnetic reconnection of Petschek type ([Petschek 1964](#); [Lyubarsky 2005](#)) develops outflows with Lorentz factors $W \sim \sigma_m^{1/2}$. Indeed, relativistic reconnection is an active area

¹ The magnetisation is defined in Heaviside-Lorentz units as $\sigma_m := B^2/(\rho W^2 c^2)$, where B , ρ , W , and c are the magnetic field strength, the rest-mass density, the bulk Lorentz factor of the plasma, and the speed of light in vacuum, respectively.

of research (Watanabe & Yokoyama 2006; Hesse & Zenitani 2007; Komissarov et al. 2007; Zenitani & Hoshino 2007; Zenitani & Hesse 2008; Zenitani et al. 2009; Tenbarge et al. 2010; Zenitani et al. 2010; Uzdensky 2011; Mizuno 2013; Takamoto 2013; Mohseni et al. 2015; Del Zanna et al. 2016; Qian et al. 2017). Reconnection outflows are bounded by shocks that any numerical code aiming to study them should handle well, in addition to current sheets and filaments in the flow. In recent years, a remarkable progress has been made in numerical methods for resistive relativistic magnetohydrodynamics (RRMHD; e.g., Komissarov 2007; Palenzuela et al. 2009; Dumbser & Zanotti 2009; Takamoto & Inoue 2011; Bucciantini & Del Zanna 2013; Takamoto 2014). The implementation of such numerical methods is chiefly based upon a conservative formulation of the RRMHD system of equations. This requires evaluating either an exact or an approximate solution to the Riemann problem at the interfaces between adjacent computational zones (see, e.g., the excellent review by Martí & Müller 2015). Exact Riemann solvers usually are computationally very expensive. Thus, approximate solvers have been broadly used in classical magnetohydrodynamics (MHD) and in relativistic MHD (RMHD) simulations. Among them, the Harten-Lax-van Leer (HLL) solver (Harten et al. 1983) has been extensively used due to its easy implementation and robustness.

Those properties of the HLL solver are based on its Jacobian-free design, which avoids the decomposition of the jumps of the characteristic variables over all right eigenvectors of the system of equations. Instead, a single state that is an average of the solution over the Riemann fan is computed. This single state is bounded by two limiting waves where Rankine-Hugoniot (RH) jump conditions hold. The higher the number of different intermediate states the Riemann problem develops (dictated by the number of different intermediate eigenvalues of the Jacobian), the less accurately the single average state over the Riemann wave structure represents the breakup of the discontinuity (i.e., the more diffusive it is). In its more basic form, the system of RRMHD equations constitutes a hyperbolic system of balance laws with two additional (elliptic) constraint equations that state the solenoidal character of the magnetic field and that the electric charge fixes the divergence of the electric field (Dixon 1978; Anile 1989). In the hyperbolic sector of the basic RRMHD system, we find 12 eigenvalues corresponding to electromagnetic waves (6 eigenvalues), fast magnetosonic waves (2 eigenvalues) and entropy, shear and charge waves (4 eigenvalues). The preservation of the elliptic constraints in RRMHD can be enforced by a suitable constraint transport method (Evans & Hawley 1988; Stone & Norman 1992) as in, e.g. Bucciantini & Del Zanna (2013). In the formulation of RRMHD of Komissarov (2007), the basic RRMHD system is *augmented* with two additional equations, that control the evolution of both scalar potentials, which act as generalised Lagrangian multipliers (GLM; Dedner et al. 2002) to maintain the constraints of the electromagnetic field. In this formulation, the constraints are not elliptic equations but, instead, hyperbolic (telegrapher) equations. Thus, in the augmented system of RRMHD, there are 14 eigenvalues, 8 of which are degenerate and equal to the speed of light (limiting the Riemann fan), in addition to two fast magnetosonic waves and four contact waves moving at the

local fluid speed (Cordero-Carrión et al. 2012). Therefore, the HLL single average state spans 3 distinct intermediate states. In contrast, the system of equations of RMHD has 5 different intermediate eigenvalues (two slow magnetosonic, one Alfvén and one contact) under non-degenerate conditions (Anile 1989; Komissarov 1999; Antón et al. 2010).

In order to ameliorate the deficiencies of the HLL-family of approximate Riemann solvers, while at the same time keeping their simplicity and computational efficiency, Toro et al. (1994) proposed a generalisation of the HLL flux for the Euler equations. These authors introduced an additional contact wave in the solution separating two intermediate states and formulated a Harten-Lax-van Leer contact (HLLC) wave approximate Riemann solver. Since then, different HLLC Riemann solvers have been designed for MHD (Gurski 2004; Li 2005) and RMHD (Mignone & Bodo 2006; Honkkila & Janhunen 2007; Kim & Balsara 2014).

In this paper, we present a new HLLC Riemann solver for the augmented system of equations of RRMHD (Sec. 2). The extra equations of the system include two scalar potentials, which control the evolution of the solenoidal constraint on the magnetic field and of the divergence of the electric field (Komissarov 2007). The new solver is implemented in a generalisation of the MRGENESIS code (Aloy et al. 1999; Miranda-Aranguren et al. 2014), which deals with the stiffness of the RRMHD equations in the ideal limit employing either Runge-Kutta Implicit-Explicit (RK-IMEX; Pareschi & Russo 2005) time integrators or Minimally Implicit Runge-Kutta (MIRK; Aloy & Cordero-Carrión 2016) methods. The solver is obtained in Sec. 4 for Resistive Special Relativistic MHD, but can be used also in applications involving General Relativistic gravitational fields resorting to the methodology devised in Pons et al. (1998). In order to demonstrate the numerical capabilities of the new HLLC solver, a number of standard one-dimensional (1D) and two-dimensional (2D) numerical tests are performed in Sec. 5. In Sec. 6, we present simulations of relativistic ideal TMs. We close this work with some concluding remarks in Sec. 7.

2 THE RRMHD EQUATIONS

A relativistic non-ideal magnetohydrodynamics fluid can be described by a system of balance laws Komissarov (2007). These equations express the conservation of charge, mass, momentum and energy, together with the Maxwell equations. In the Heaviside-Lorentz units used in this paper, with the speed of light $c = 1$, these equations read:

$$\partial_t q = -\nabla \cdot \mathbf{J}, \quad (1)$$

$$\partial_t \psi = -\nabla \cdot \mathbf{E} + q - \kappa \psi, \quad (2)$$

$$\partial_t \phi = -\nabla \cdot \mathbf{B} - \kappa \phi, \quad (3)$$

$$\partial_t \mathbf{E} = \nabla \times \mathbf{B} - \nabla \psi - \mathbf{J}, \quad (4)$$

$$\partial_t \mathbf{B} = -\nabla \times \mathbf{E} - \nabla \phi, \quad (5)$$

$$\partial_t D = -\nabla \cdot \mathbf{F}_D, \quad (6)$$

$$\partial_t \mathcal{E} = -\nabla \cdot \mathbf{F}_\tau, \quad (7)$$

$$\partial_t \mathbf{S} = -\nabla \cdot \mathbf{F}_S, \quad (8)$$

where q , $\mathbf{E} = (E_x, E_y, E_z)^T$, $\mathbf{B} = (B_x, B_y, B_z)^T$, D , \mathcal{E} and \mathbf{S} stand for the charge density, the electric and magnetic

field 3-vectors in the laboratory frame, the relativistic mass-density, the relativistic energy density and the momentum density, respectively. We use a divergence cleaning strategy (Dedner et al. 2002), where the scalar pseudopotentials ψ and ϕ enforce the conservation of q and of the solenoidal constrain $\nabla \cdot \mathbf{B} = 0$, respectively. These pseudopotentials decay exponentially with time if the constant $\kappa := c_h^2/c_p^2 > 0$, where c_p^2 can be regarded as a diffusion coefficient and c_h as the finite speed at which $\nabla \cdot \mathbf{B}$ errors propagate. For simplicity and not to limit further the time step, we choose this finite speed equal to speed of light ($c_h = 1$) and following Mignone & Tzeferacos (2010), we define the dimensionless parameter,

$$\alpha := \Delta h \frac{c_h}{c_p^2},$$

where $\Delta h := \min(\Delta x, \Delta y, \Delta z)$, and $\Delta x, \Delta y, \Delta z$ are the grid spacings in the three Cartesian directions. According to Mignone & Tzeferacos (2010), the errors associated with the violation of the magnetic field solenoidal constrain are minimised when $\alpha \in [0, 1]$. In the numerical experiments presented in this work (Sec. 5), we set $\alpha = 1$.

The *augmented* system of RRMHD equations (1)–(8), can be written as a system of balance laws:

$$\partial_t \mathbf{U} + \sum_k \partial_k \mathbf{F}(\mathbf{U}) = \boldsymbol{\Omega}(\mathbf{U}), \quad (9)$$

where \mathbf{U} , \mathbf{F} and $\boldsymbol{\Omega}$ are the conserved variables, the fluxes and the source terms, respectively. The vector $\mathbf{U} = (\psi, \phi, \mathbf{E}, \mathbf{B}, q, D, \mathcal{E}, \mathbf{S})^T$ of conserved variables is related to the vector of primitive or physical variables $\mathbf{W} = (\psi, \phi, \mathbf{E}, \mathbf{B}, q, \rho, p_g, \mathbf{v})^T$ through the following algebraic relations:²

$$D = \rho W, \quad (10)$$

$$\mathcal{E} = \mathcal{E}_{\text{EM}} + \mathcal{E}_{\text{hyd}} = \frac{1}{2}(\mathbf{E}^2 + \mathbf{B}^2) + \rho h W^2 - p_g, \quad (11)$$

$$\mathbf{S} = \mathbf{S}_{\text{EM}} + \mathbf{S}_{\text{hyd}} = \mathbf{E} \times \mathbf{B} + \rho h W^2 \mathbf{v}, \quad (12)$$

where p_g is the gas pressure, ρ the proper rest mass density, $\mathbf{v} = (v_x, v_y, v_z)^T$ the fluid velocity measured in laboratory frame, $W = (1 - \mathbf{v}^2)^{-1/2}$ the Lorentz factor and $h = 1 + \varepsilon + p_g/\rho$ the specific enthalpy, ε being the specific energy. For an ideal gas equation of state with constant adiabatic index γ , $p = (\gamma - 1)\rho\varepsilon$, the specific enthalpy can be written as

$$h(\rho, p) = 1 + \frac{\gamma}{\gamma - 1} \frac{p}{\rho},$$

and the local sound speed reads $c_s = \sqrt{\gamma p/(\rho h)}$. The system (9) is hyperbolic if $\partial_\varepsilon p_g - \rho c_s^2 \neq 0$ (Cordero-Carrión et al. 2012).

The fluxes can be explicitly written in terms of the primi-

² The subset of values $\{\phi, \psi, \mathbf{E}, \mathbf{B}, q\}$ can be regarded as both conserved or primitive variables.

тиве variables:

$$\begin{aligned} \mathbf{F}_q &= \mathbf{J}, \\ \mathbf{F}_\psi &= \mathbf{E}, \\ \mathbf{F}_\phi &= \mathbf{B}, \\ F_{E^i}^j &= \delta_i^j \psi - \epsilon_{ijk} B^k, \\ F_{B^i}^j &= \delta_i^j \phi + \epsilon_{ijk} E^k, \\ \mathbf{F}_D &= \rho W \mathbf{v}, \\ \mathbf{F}_\mathcal{E} &= \mathbf{E} \times \mathbf{B} + \rho h W^2 \mathbf{v}, \\ \mathbf{F}_\mathbf{S} &= -\mathbf{E} \mathbf{E} - \mathbf{B} \mathbf{B} + \rho h W^2 \mathbf{v} \mathbf{v} + P \mathbf{g}, \end{aligned} \quad (13)$$

where $P = p_g + (\mathbf{E}^2 + \mathbf{B}^2)/2$ is the total pressure, $\mathbf{g} = \text{diag}(-1, 1, 1, 1)$ is the Minkowski metric tensor and δ_i^j and ϵ_{ijk} are the Kronecker delta and the Levi-Civita symbol, respectively. The source term is given by $\boldsymbol{\Omega} = (q - \kappa\psi, -\kappa\phi, -\mathbf{J}, \mathbf{0}_{1 \times 9})^T$, where $\mathbf{J} = (J_x, J_y, J_z)^T$ is the electric current density, which employing the Ohm's law takes the form (Komissarov 2007)

$$\mathbf{J} := \mathbf{J}_s + q \mathbf{v} = \sigma W [\mathbf{E} + \mathbf{v} \times \mathbf{B} - (\mathbf{E} \cdot \mathbf{v}) \mathbf{v}] + q \mathbf{v}, \quad (14)$$

where σ is the electrical conductivity of the medium. In the ideal case (i.e., $\sigma \rightarrow \infty$) the resistive part (\mathbf{J}_s) of the total electric current density makes the system of RRMHD equations stiff. In that limit, the characteristic time scale ($1/\sigma$) of the source term ($\boldsymbol{\Omega}$) is, in general, much shorter than the timescale of hyperbolic part (\mathbf{F}). This may introduce instabilities in the time integration if an explicit method is directly used. We face these possibility employing implicit-explicit methods. In particular, we may use either RK-IMEX (Palenzuela et al. 2009) or MIRK (Aloy & Cordero-Carrión 2016) schemes. In the case of using an RK-IMEX scheme, the source vector $\boldsymbol{\Omega}$ is split into both a stiff and a non-stiff operators, which read, $\boldsymbol{\Omega}_s = (0, 0, -\mathbf{J}_s, \mathbf{0}_{1 \times 9})$ and $\boldsymbol{\Omega}_{ns} = (q - \kappa\psi, -\kappa\phi, -q\mathbf{v}, \mathbf{0}_{1 \times 9})$, respectively.

Note that in Eqs. (11) and (12), we explicitly write the total conserved energy density and momentum density as the sum of two independent contributions, electromagnetic (subscript ‘‘EM’’) and purely hydrodynamic (subscript ‘‘hyd’’). In the case of using a MIRK time integration scheme, the recovery of the primitive variables from the conserved ones reduces to the same algorithm as for the relativistic Euler equations (Aloy et al. 1999, App. C), taking as conserved variables the subset $\{D, \mathbf{S}_{\text{hyd}}, \tau_{\text{hyd}}\} = \{D, \mathbf{S} - \mathbf{S}_{\text{EM}}, \mathcal{E} - \mathcal{E}_{\text{EM}} - D\}$. This is because, firstly, the subset of variables $\{\phi, \psi, \mathbf{E}, \mathbf{B}, q\}$ are both conserved and primitive variables and, secondly, the RRMHD system includes both equations for \mathbf{E} (Eq. 4) and \mathbf{B} (Eq. 5). We note, however, that for generic RK-IMEX time integration schemes, the simplest version of the procedure to recover variables cannot be directly used. Instead, we resort to the procedure delineated in Sec. 4.2 of Palenzuela et al. (2009).

3 CHARACTERISTIC SPEEDS

We consider for simplicity a Riemann problem along the x -coordinate direction set at the location $x_{i+1/2}$, i.e., the interface between two consecutive cells, i and $i + 1$

$$\mathbf{U}(x, 0) = \begin{cases} \mathbf{U}_l & \text{if } x < x_{i+1/2} \\ \mathbf{U}_r & \text{if } x > x_{i+1/2}, \end{cases}$$

where \mathbf{U}_l and \mathbf{U}_r are the initial (uniform) states to the left and to the right of $x_{i+1/2}$. The breakup of this Riemann problem in RRMHD produces a set of 14 waves with characteristic speeds

$$\lambda_{EB\pm} = \pm 1, \quad (\text{multiplicity 4}) \quad (15)$$

$$\lambda_q = v_x, \quad (\text{multiplicity 1}) \quad (16)$$

$$\lambda_{H_0} = v_x, \quad (\text{multiplicity 3}) \quad (17)$$

$$\lambda_{H\pm} = v_x \Delta_H \pm c_s \sqrt{\frac{\rho h}{\Delta}} (1 - v_x^2 \Delta_H), \quad (\text{multiplicity 1}) \quad (18)$$

where $\Delta := \rho h W^2 (1 - \mathbf{v}^2 c_s^2)$, and $\Delta_H := (1 - c_s^2) / (1 - \mathbf{v}^2 c_s^2)$ (Cordero-Carrión et al. 2012).

We point out that the characteristic speeds listed in Eqs. (15)-(18) are computed, following the standard practice for hyperbolic systems of partial differential equations (e.g., Anile 1989) as the eigenvalues of the Jacobian matrices of the system of RRMHD equations. These eigenvalues represent the wave speeds of plasma perturbations only in the infinite resistivity limit. This is the reason why Alfvén and slow magnetosonic waves do not explicitly appear among the obtained characteristic speeds. The presence of source terms (the current in Ampere's law; Eq. (4) and the GLM scalar potentials in Eqs. (2) and (3)) alters these signal velocities. Indeed, both the basic and the augmented RRMHD systems belong to the class of "hyperbolic systems of conservation laws with relaxation" as defined by, e.g., Whitham (1974). The latter term denotes hyperbolic systems of n partial differential equations in conservation form with source terms, which have as a limit a hyperbolic system of M ($M < n$) equations called the equilibrium system as $n - M$ relaxation time parameters $\tau_i \rightarrow 0$. In our case, the equilibrium system is the one formed by the equations of (ideal) RMHD and the relaxation parameters are the resistivity, $\eta := 1/\sigma$, and $1/\kappa$. Following the convention of Pember (1993), the characteristic speeds of the equilibrium and non-equilibrium systems are called *equilibrium* and *frozen* characteristic speeds, respectively.³

The equilibrium ($\tilde{\lambda}_j$, $j = 1, \dots, M$) and frozen (λ_j , $j = 1, \dots, n$) characteristic speeds satisfy the *subcharacteristic condition* if they are interlaced, i.e., if each $\tilde{\lambda}_j$ lies in the closed interval $[\lambda_k, \lambda_{k+n-M}]$. The previous condition is necessary for the stability of linearised systems with relaxation (Whitham 1974). The subcharacteristic condition is satisfied by the characteristic speeds of both the basic and the augmented RRMHD systems and the characteristic speeds of the (ideal) RMHD system. Therefore, the numerical solution of the former systems tends to the solution of the equilibrium (ideal RMHD) system as the relaxation time tends to zero (Chen et al. 1994). The eigenspeeds computed by Cordero-Carrión et al. (2012) only apply to the frozen limit where electromagnetic phenomena and matter are completely decoupled. However, the coupling is restored by our method of lines and the application of partly implicit time integration methods (either RKIMEX or MIRK).

³ One can actually define the concept of stiffness in this framework saying that a system of conservation laws is stiff when at least one of its relaxation times is small compared to the time scale determined by the frozen characteristic speeds of the system and some appropriate length scale.

Takamoto & Inoue (2011) took an alternative approach employing a method of characteristics (MOC) for the integration of the RRMHD equations. Alfvén modes are explicitly restored in their approach Takamoto & Inoue (2011) by modifying Ampere's law introducing an effective propagation speed, which depends on the damping rate of electromagnetic modes. That is, when all electromagnetic modes (moving at the speed of light) are damped during one time step of the numerical evolution, Δt , they use appropriate (ideal RMHD) characteristic speeds for their MOC; otherwise, they resort to using the speed of light. In practice, the method of Takamoto & Inoue (2011) only uses characteristic speeds smaller than the speed of light when $\Delta t < \Delta t_e := 4\pi/\sigma$. Our partly implicit time integration methods typically provide values of $\Delta t = C_{\text{CFL}} \Delta x \gg \Delta t_e$ for reasonable values of the grid spacing. This means that our algorithm should yield a qualitatively similar restoration of the Alfvén, fast and slow RMHD modes as that of Takamoto & Inoue (2011) in practical applications.

4 HLLC SOLVER

An HLLC approximate Riemann solver avoids the full characteristic decomposition of all the wave pattern in the Riemann fan by only introducing a contact wave with constant speed, λ^* , which separates two intermediate states $(\mathbf{U}_l^*, \mathbf{U}_r^*)$ bounded by two fast shocks. More explicitly, the solution of the initial value problem in each cell interface is written as

$$\mathbf{U}(0, t) = \begin{cases} \mathbf{U}_l & \text{if } \lambda_l \geq 0 \\ \mathbf{U}_l^* & \text{if } \lambda_l < 0 \leq \lambda^* \\ \mathbf{U}_r^* & \text{if } \lambda^* < 0 \leq \lambda_r \\ \mathbf{U}_r & \text{if } \lambda_r < 0, \end{cases} \quad (19)$$

where λ^* is the propagation velocity of the contact wave and λ_l, λ_r are estimates of the maximum signal speeds propagating to the left and to the right of the initial discontinuity, respectively. Since in RRMHD the electromagnetic fields propagate at the speed of light (Eq. 15), we set $\lambda_l = -1$ and $\lambda_r = 1$, but for sake of clarity, we maintain the notation λ_l, λ_r throughout the paper.

The numerical fluxes corresponding to the assumed solution (19) are:

$$\tilde{\mathbf{F}} = \begin{cases} \mathbf{F}_l & \text{if } \lambda_l \geq 0 \\ \mathbf{F}_l^* & \text{if } \lambda_l < 0 \leq \lambda^* \\ \mathbf{F}_r^* & \text{if } \lambda^* < 0 \leq \lambda_r \\ \mathbf{F}_r & \text{if } \lambda_r < 0, \end{cases} \quad (20)$$

with $\mathbf{F}_l = \mathbf{F}(\mathbf{U}_l)$ and $\mathbf{F}_r = \mathbf{F}(\mathbf{U}_r)$ and $\mathbf{F}_l^*, \mathbf{F}_r^*$ the intermediate flux functions, whose expressions will be found in the next subsections.

4.1 Rankine-Hugoniot conditions for a bounded source term

Following LeVeque (2002), a one-dimensional, scalar balance law, $\partial_t U(x, t) + \partial_x F(U(x, t)) = \Omega(x, t)$, can be expressed in

integral form as:

$$\begin{aligned} \int_{x_1}^{x_1+\Delta x} U(x, t_1 + \Delta t) dx - \int_{x_1}^{x_1+\Delta x} U(x, t_1) dx = \\ \int_{t_1}^{t_1+\Delta t} F(U(x_1, t) dt - \int_{t_1}^{t_1+\Delta t} F(U(x_1 + \Delta x, t) dt \\ + \int_{t_1}^{t_1+\Delta t} \int_{x_1}^{x_1+\Delta x} \Omega(x, t) dx dt, \quad (21) \end{aligned}$$

where the integration domain is $[t_1, t_1 + \Delta t] \times [x_1, x_1 + \Delta x]$. If the source term $\Omega(x, t)$ is a bounded function, the last integral in (21) can be expressed in terms of the characteristic velocity of the balance law, λ , as,

$$\begin{aligned} \int_{t_1}^{t_1+\Delta t} \int_{x_1}^{x_1+\Delta x} \Omega(x, t) dx dt \approx \Delta t \Delta x \Omega(x, t) \\ \approx \Delta t^2 \lambda \Omega(x, t). \quad (22) \end{aligned}$$

Thus, from the conservation law defined in (21) the RH conditions in vectorial form, can be written as:

$$\lambda(\mathbf{U}_r - \mathbf{U}_l) \approx \mathbf{F}_r - \mathbf{F}_l + \lambda \Delta t \Omega,$$

which is an expression of the order $\mathcal{O}(\Delta t)$ and the contribution of the source term vanishes as $\Delta t \rightarrow 0$. Hence, a bounded source term does not change the RH conditions at a discontinuity and, thus, we can use the following set of RH conditions for the shocks and contact wave in the HLLC solution:

$$\lambda_l(\mathbf{U}_l^* - \mathbf{U}_l) = \mathbf{F}_l^* - \mathbf{F}_l, \quad (23)$$

$$\lambda^*(\mathbf{U}_r^* - \mathbf{U}_l^*) = \mathbf{F}_r^* - \mathbf{F}_l^*, \quad (24)$$

$$\lambda_r(\mathbf{U}_r - \mathbf{U}_r^*) = \mathbf{F}_r - \mathbf{F}_r^*. \quad (25)$$

4.2 HLLC consistency conditions

Following Mignone & Bodo (2006), we find the consistency conditions for conserved intermediate variables by adding the tree equations in (23)-(25),

$$\frac{(\lambda^* - \lambda_l) \mathbf{U}_l^* + (\lambda_r - \lambda^*) \mathbf{U}_r^*}{\lambda_r - \lambda_l} = \mathbf{U}^{\text{hll}}, \quad (26)$$

where

$$\mathbf{U}^{\text{hll}} = \frac{\lambda_r \mathbf{U}_r - \lambda_l \mathbf{U}_l + \mathbf{F}_l - \mathbf{F}_r}{\lambda_r - \lambda_l},$$

is the (HLL) integral average of the solution of the Riemann problem over the wave fan (cf. Toro 1997, § 10.4). Likewise, dividing each equation in (23)-(25) by their corresponding λ on the left-hand sides and adding all the resulting expressions one finds

$$\frac{(\lambda^* - \lambda_l) \lambda_r \mathbf{F}_l^* + (\lambda_r - \lambda^*) \lambda_l \mathbf{F}_r^*}{\lambda_r - \lambda_l} = \lambda^* \mathbf{F}^{\text{hll}} \quad (27)$$

with

$$\mathbf{F}^{\text{hll}} = \frac{\lambda_r \mathbf{F}_l - \lambda_l \mathbf{F}_r + \lambda_r \lambda_l (\mathbf{U}_r - \mathbf{U}_l)}{\lambda_r - \lambda_l} \quad (28)$$

being the (HLL) flux integral average of the solution over the Riemann wave structure. We point out that employing the (global) values for the system limiting speeds $\lambda_l = -1$ and $\lambda_r = +1$, the HLL flux (28) reduces to the Local Lax-Friedrich flux.

Building an HLLC solver for the RRMHD system of

equations ultimately amounts to obtaining the expressions of \mathbf{F}_l^* and \mathbf{F}_r^* in (20). In general, $\mathbf{F}_l^* \neq \mathbf{F}(\mathbf{U}_l^*)$ and $\mathbf{F}_r^* \neq \mathbf{F}(\mathbf{U}_r^*)$. Instead, the RH jump conditions (24) provide a set of relations between the starred numerical fluxes and the corresponding state vectors \mathbf{U}_l^* and \mathbf{U}_r^* . More precisely, if \mathbf{U}_l^* and \mathbf{U}_r^* are known, from Eqs. (23) and (25), we have

$$\begin{aligned} \mathbf{F}_l^* &= \mathbf{F}_l + \lambda_l (\mathbf{U}_l^* - \mathbf{U}_l), \\ \mathbf{F}_r^* &= \mathbf{F}_r + \lambda_r (\mathbf{U}_r^* - \mathbf{U}_r). \end{aligned} \quad (29)$$

If each state vector has n components ($n = 14$ in the RRMHD system of equations (1)–(8)), the problem at hand has $4n + 1$ unknowns, i.e. \mathbf{F}_l^* , \mathbf{F}_r^* , \mathbf{U}_l^* , \mathbf{U}_r^* , and λ^* . In addition, there are four ancillary variables, $v_{x,r}^*$, $v_{x,l}^*$, P_r^* and P_l^* , originating from the fact that the fluxes (Eq. 13) cannot be expressed in closed form only as a function of the conserved variables. However, if we include these ancillary variables as a part of our problem, the momentum in the x –direction is not an independent variable, since using Eqs. (11) and (12), it can be written as

$$S_{x,a}^* = (\mathbf{E}_a^* \times \mathbf{B}_a^*)_x + (\mathcal{E}_a^* + P_a^* - (\mathbf{E}_a^*)^2 - (\mathbf{B}_a^*)^2) v_{x,a}^*, \quad (30)$$

where the subscript $a = l, r$ refers to each of the two states to the left and to the right of the contact wave. Thus, we have to find $4n + 5$ relations among the unknowns. Two of them are provided by Eq. (30). There are $2n$ consistency relations (26) and (27). We advance that part of the n RH conditions across the middle wave (Eq. 24) become trivially satisfied (and thus replaced) by the subsequent assumptions that we employ to find the remaining $2n + 3 (= 31)$ equations. We chose these additional equations in the following way. First, we assume the continuity of a subset of the conserved variables and of the four ancillary variables. Second, we assume the functional dependence of the fluxes in the starred regions with the conserved and ancillary variables. Specifically, we impose continuity of the charge density, of the scalar potentials ϕ and ψ as well as of the magnetic and electric field components across the contact wave,

$$\begin{aligned} q_r^* &= q_l^* := q^*, & B_{i,r}^* &= B_{i,l}^* := B_i^*, & E_{i,r}^* &= E_{i,l}^* := E_i^*, \\ \phi_r^* &= \phi_l^* := \phi^*, & \psi_r^* &= \psi_l^* := \psi^*, \end{aligned} \quad (31)$$

where $i = x, y, z$. For the ancillary variables, we impose continuity of the total pressure and of the normal component of the velocity, i.e.,

$$P_r^* = P_l^* := P^*, \quad v_{x,r}^* = v_{x,l}^* = \lambda^*. \quad (32)$$

The conditions imposed on the conserved variables (Eq. 31) provide 9 relations among the unknowns of our problem, to which we add the 9 non-trivial RH conditions across the middle wave corresponding to the same subset of conserved variables (i.e., q^* , ϕ^* , ψ^* , \mathbf{E}^* and \mathbf{B}^*), as well as the additional three conditions (Eq. 32) on the ancillary variables. Therefore, there are still 10 additional missing equations to set a well posed problem, which come from assuming that the form of the fluxes \mathbf{F}^* formally is the same as that of Eq. (13) in the x –direction for the following set of variables $(D^*, S_x^*, S_y^*, S_z^*, \mathcal{E}^*)$. More precisely, we assume that

the starred fluxes relate to the starred variables through

$$F_{D,a}^* = D_a^* \lambda^*, \quad (33)$$

$$F_{\mathcal{E},a}^* = S_{x,a}^*, \quad (34)$$

$$F_{S_x,a}^* = -E_x^* E_x^* - B_x^* B_x^* + [S_{x,a}^* - (\mathbf{E}^* \times \mathbf{B}^*)_x] \lambda^* + P^*, \quad (35)$$

$$F_{S_y,a}^* = -E_x^* E_y^* - B_x^* B_y^* + [S_{y,a}^* - (\mathbf{E}^* \times \mathbf{B}^*)_y] \lambda^*, \quad (36)$$

$$F_{S_z,a}^* = -E_x^* E_z^* - B_x^* B_z^* + [S_{z,a}^* - (\mathbf{E}^* \times \mathbf{B}^*)_z] \lambda^*. \quad (37)$$

The assumed dependence of the fluxes on the conserved variables and on the λ^* and P^* makes that 5 RH conditions across the contact wave (Eq. 24) corresponding to the subset of variables $(D^*, S_x^*, S_y^*, S_z^*, \mathcal{E}^*)$ become trivially satisfied. Hence, these equations are replaced by Eqs. (33)-(37).

For the subset of conserved variables for which we have assumed continuity across the contact wave (Eq. 31), the consistency condition (26) yields:

$$\begin{aligned} q^* &= q^{\text{hll}}, & B_i^* &= B_i^{\text{hll}}, & E_i^* &= E_i^{\text{hll}}, \\ \phi^* &= \phi^{\text{hll}}, & \psi^* &= \psi^{\text{hll}}. \end{aligned} \quad (38)$$

The fluxes corresponding to the conserved variables given in (38) are readily found applying Eqs. (29):

$$\begin{aligned} F_{q,a}^* &= F_q^{\text{hll}}, & F_{\phi,a}^* &= F_\phi^{\text{hll}}, & F_{\psi,a}^* &= F_\psi^{\text{hll}}, \\ F_{B_i,a}^* &= F_{B_i}^{\text{hll}}, & F_{E_i,a}^* &= F_{E_i}^{\text{hll}}. \end{aligned} \quad (39)$$

The flux of \mathcal{E}_a^* is exactly $S_{x,a}^*$ (Eq. 34) and, hence, employing the consistency relations (27) and (26), we find

$$S_{x,a}^* = \frac{\lambda_a S_x^{\text{hll}} - \lambda^* F_{\mathcal{E}}^{\text{hll}}}{\lambda_a - \lambda^*}. \quad (40)$$

Similarly, the especially simple form of the flux of D (Eq. 33), inserted in any of the Eqs. (29), yields:

$$D_a^* = \frac{\lambda_a - v_{x,a}}{\lambda_a - \lambda^*} D_a. \quad (41)$$

Using relation (27) for the y - and z -momentum density fluxes (Eqs. 36 and 37) combined with Eq. (26) for S_y^{hll} and S_z^{hll} yields

$$\begin{aligned} S_{y,a}^* &= \frac{\lambda_a S_y^{\text{hll}} - F_{S_y}^{\text{hll}} - \lambda^* (\mathbf{E}^* \times \mathbf{B}^*)_y - E_x^* E_y^* - B_x^* B_y^*}{\lambda_a - \lambda^*}, \\ S_{z,a}^* &= \frac{\lambda_a S_z^{\text{hll}} - F_{S_z}^{\text{hll}} - \lambda^* (\mathbf{E}^* \times \mathbf{B}^*)_z - E_x^* E_z^* - B_x^* B_z^*}{\lambda_a - \lambda^*}. \end{aligned} \quad (42)$$

Applying the consistency relation (26) to the x component of the momentum density, we find

$$S_x^{\text{hll}} = \lambda^* [\mathcal{E}^{\text{hll}} + P^* - (\mathbf{E}^*)^2 - (\mathbf{B}^*)^2] + (\mathbf{E}^* \times \mathbf{B}^*)_x. \quad (43)$$

Likewise, applying the consistency relation (27) to the x component of the momentum density flux (35) and to the energy density flux (34) yields

$$\lambda^* F_{S_x}^{\text{hll}} = (\lambda^*)^2 [F_{\mathcal{E}}^{\text{hll}} - (\mathbf{E}^* \times \mathbf{B}^*)_x] + \lambda^* [P^* - (E_x^*)^2 - (B_x^*)^2]. \quad (44)$$

Subtracting Eq. (44) from Eq. (43) we arrive at a quadratic equation for λ^*

$$a(\lambda^*)^2 + b\lambda^* + c = 0, \quad (45)$$

whose coefficients are

$$\begin{aligned} a &= F_{\mathcal{E}}^{\text{hll}} - (\mathbf{E}^* \times \mathbf{B}^*)_x, \\ b &= (\mathbf{E}_\perp^*)^2 + (\mathbf{B}_\perp^*)^2 - \mathcal{E}^{\text{hll}} - F_{S_x}^{\text{hll}}, \\ c &= S_x^{\text{hll}} - (\mathbf{E}^* \times \mathbf{B}^*)_x, \end{aligned} \quad (46)$$

where $(\mathbf{B}_\perp^*) = (0, B_y^*, B_z^*)^T$ and $\mathbf{E}_\perp^* = (0, E_y^*, E_z^*)^T$.

In the ideal limit, in which the electric field simply is $\mathbf{E} = -\mathbf{v} \times \mathbf{B}$, the coefficients of the quadratic equation (46) reduce to the expressions in Mignone & Bodo (2006). Thus, employing the same arguments as in the former paper (see also Mignone & Bodo 2005), of the two roots of Eq. (45), only the one with the minus sign is compatible with $\lambda_l \leq \lambda^* \leq \lambda_r$ and, therefore, it is the physically admissible solution.

If the solution resulting from Eq. (45) is $\lambda^* \neq 0$, then P^* can be recovered from Eq. (44)

$$P^* = F_{S_x}^{\text{hll}} + (E_x^*)^2 + (B_x^*)^2 - \lambda^* [F_{\mathcal{E}}^{\text{hll}} - (\mathbf{E}^* \times \mathbf{B}^*)_x]. \quad (47)$$

In the complementary case that $\lambda^* = 0$, using the second RH condition of (24) together with the flux consistency condition (27) allows us to express all the fluxes in terms of the HLL flux (i.e., in terms of the variables in the left and right states):

$$\mathbf{F}_r^* = \mathbf{F}_l^* = \mathbf{F}^{\text{hll}} \quad (\text{if } \lambda^* = 0), \quad (48)$$

and the calculation of P^* is not necessary to obtain the numerical fluxes.

The energy density \mathcal{E} (Eq. 11), can also be expressed as

$$\mathcal{E} = (S_x - (\mathbf{E} \times \mathbf{B})_x)/v_x - P + \mathbf{E}^2 + \mathbf{B}^2,$$

if $v_x \neq 0$. In any of the intermediate states, using Eq. (40), we find:

$$\mathcal{E}_a^* = \frac{1}{\lambda^*} \left[\frac{\lambda_a S_x^{\text{hll}} - \lambda^* F_{\mathcal{E}}^{\text{hll}}}{\lambda_a - \lambda^*} - (\mathbf{E}^* \times \mathbf{B}^*)_x \right] - P^* + (\mathbf{E}^*)^2 + (\mathbf{B}^*)^2, \quad (49)$$

if $\lambda^* \neq 0$. The complementary case ($\lambda^* = 0$) makes use of Eq. (48), and the evaluation of \mathcal{E}_a^* is not needed.

4.3 Discussion of the assumptions made to build the HLLC solver

Notice that in equation Eq. 32, we have assumed that the speed of the contact wave is equal to the (average) normal velocity over the Riemann fan. We point out that one may choose different sets of variables to be continuous across the contact wave. Our choice is similar (but not equal) to that of Mignone & Bodo (2006). However, we do not impose continuity of the components of the velocity parallel to the contact wave. In this sense, our approach is similar to that of Li (2005) in classical MHD or to the one of Honkkila & Janhunen (2007) or Kim & Balsara (2014) in RMHD. Instead, we impose continuity of the electric field due to its duality with respect to the magnetic field in RRMHD.

We have also imposed continuity of the scalar potentials ϕ_a^* and ψ_a^* and left unspecified the form of their corresponding fluxes, $F_{\phi,a}^*$ and $F_{\psi,a}^*$, respectively, which are unknowns of the problem. If we did not assume continuity of ϕ^* and ψ^* , this would be incompatible with the RH conditions across

the middle wave (Eq. 24) if we also enforced that $F_{\phi,a}^* = B_x^*$ and that $F_{\psi,a}^* = E_x^*$. Alternatively, we could relax the conditions $\phi_r^* = \phi_l^*$ and $\psi_r^* = \psi_l^*$ and assume that $F_{\phi,a}^* = B_x^*$ and $F_{\psi,a}^* = E_x^*$, but then the resulting system of equations becomes overdetermined. In the practical applications where we have used the new HLLC solver, this is not a problem though. The reason is that if we assume that the form of the fluxes of ϕ_a^* and ψ_a^* is $F_{\phi,a}^* = B_x^*$ and $F_{\psi,a}^* = E_x^*$, we obtain from the RH conditions across the middle wave that $\phi_r^* = \phi_l^*$ and $\psi_r^* = \psi_l^*$. But then, we have two alternative expressions for the fluxes of the latter variables: from the consistency relations across the outermost waves (Eqs. 26 and 27), we have $F_{\phi,a}^* = F_\phi^{\text{hll}}$ and $F_{\psi,a}^* = F_\psi^{\text{hll}}$, while from the assumed form of the fluxes, we obtain $F_{\phi,a}^* = B_x^{\text{hll}}$ and $F_{\psi,a}^* = E_x^{\text{hll}}$, respectively. These alternative expressions for the fluxes are in general incompatible. There is, however, a possibility to make all these alternative expressions of the fluxes in the starred region compatible if and only if $\lambda_l = -1$ and $\lambda_r = +1$. Fortunately, this is the default choice that we make for the bounds on the limiting speeds of the RRMHD system. However, this procedure leaves no choice on the selection of λ_l and λ_r , as it is typically the case in other HLLC solvers. Another way to circumvent the incompatibility found above (if we do not enforce $\phi_r^* = \phi_l^*$ and $\psi_r^* = \psi_l^*$) is to assume that the fluxes of ϕ^* and ψ^* are free variables. However, to close the system of equations, we would need to impose two additional relations among the fluxes of ϕ^* and ψ^* on each side of the middle wave. In this regard, two considerations are in order. First, the scalar potentials are introduced in the algorithm to preserve the constraints $\nabla \cdot \mathbf{E} = q$ and $\nabla \cdot \mathbf{B} = 0$ and, second, we assume that both \mathbf{E} and \mathbf{B} are continuous across the middle wave. Taking into account these two considerations, we have not found satisfactory alternatives to the assumption of continuity of the ϕ^* and ψ^* across the contact wave in the standard framework of an HLLC solver for the whole set of conserved variables (but see App. A).

5 NUMERICAL EXPERIMENTS

In this section, we demonstrate the performance of the new HLLC solver in a number of 1D Riemann problems and 2D standard (R)RMHD tests. To compare our results with the ones in the ideal limit, we set the conductivity to a large constant value, i.e. $\sigma = 10^6$ (see the discussion in Sec. 5.4 as well as Fig. 10). All 1D test problems are performed in a computational domain $x \in [0, 1]$ with and the CFL factor $C_{\text{CFL}} = 0.1$. The initial discontinuity is placed at $x = 0.5$. RRMHD equations are integrated using the second order MIRK method (Aloy & Cordero-Carrión 2016). However, we note that most of the results presented in this paper are computed employing a (globally) 1st-order accurate scheme, resulting from not applying any intercell reconstruction to the numerical variables (Godunov method). In this way, a comparison of the performance of the HLL and HLLC Riemann solvers can be shown more clearly. The initial conditions for 1D tests are summarised in Tab. 1.

5.1 Contact Wave Discontinuities (CW1, CW2)

Contact wave discontinuity tests (CW1 and CW2 in Tab. 1) consist in simulating an isolated contact discontinuity with

a jump only in the mass density ρ . In the CW1 test, where $v_x = 0$, the HLLC solver does not show any smearing of the initial profile, as for this particular case, HLLC resolves the discontinuity (Fig. 1 left panel) exactly. This behaviour is expected for the HLLC solver, which is specifically built to include a contact wave in the numerical solution. In the CW2 test, whose setup was proposed by Honkkila & Janhunen (2007), there is a smearing of the contact wave, which is smaller for the HLLC solver than for the HLL solver (Fig. 1 central panel). The smearing of the contact wave is a result of two facts: (i) the non-Lorentzian invariance of the numerical viscosity added by the HLL and HLLC solvers; (ii) an inherent numerical diffusion of shock-capturing methods of Godunov-type (unless specific techniques to track internal interfaces dynamics are employed; see, e.g., Abgrall & Karni 2001).

We have considered several variants of the CW2 test where progressively larger values of v_x are taken. As $v_x \rightarrow 1$, the diffusion of the contact discontinuity becomes larger in both approximate Riemann solvers and the differences between them reduce (yet the HLLC solver always displays smaller smearing than the HLL solver). This is due to the degeneration of the Riemann structure when any of the components of the 3-velocity is close to the speed of light. Under such conditions, all eigenvalues of the system of RRMHD equations approach the speed of light and the contact wave is resolved as a shock by the algorithm (thus, unphysical numerical dissipation is added).

5.2 Rotational Wave (RW)

Following (Mignone et al. 2009), we set up an isolated rotational wave like in their ideal RMHD test. Across a rotational wave, the components of vector fields exhibit jumps (yet their moduli are preserved), while scalar quantities (e.g., rest-mass density, total pressure, etc.) are continuous. We show in Fig. 2 the variation of B_y across the rotational wave. Neither the HLL nor the HLLC solver is able to capture the initially specified jump (see Tab. 1) and both smear the solution (the HLL solver slightly more than the HLLC solver).

As noted in Antón et al. (2010), in practical applications, the numerical diffusion is not as large as one may infer from the results of Fig. 2 (upper panel). To ameliorate the problem, a high-order spatial interpolation (instead of using simply the Godunov method) is advisable. Thus, we have repeated both the RW and also the CW2 tests employing a 5th-order monotonicity-preserving (MP5) intercell reconstruction (Suresh & Huynh 1997). The results are shown in Figs. 1 (right panel) and 2 (bottom panel). In both cases, only 4 numerical zones are needed to resolve the isolated discontinuities.

5.3 Shock Tube Problem 1 (ST1)

The test of Balsara (2001) (which is a relativistic extension of the test proposed by Brio & Wu 1988) has been used by a number of practitioners in the RMHD field (e.g., Del Zanna et al. 2003; Leismann et al. 2005; Mignone & Bodo 2006; Mignone et al. 2009; Antón et al. 2010). It considers a fluid with adiabatic index $\gamma = 2$.

Table 1. Initial conditions for 1D test problems. In all simulations, we set the pseudopotentials and the charge density to zero, i.e. $\psi = \phi = q = 0$, and the electric field to its ideal approximation $\mathbf{E} = -\mathbf{v} \times \mathbf{B}$. The columns give the test name, the state (left; L or right; R), rest-mass density ρ , gas pressure p_g , velocity and magnetic field components (\mathbf{v} and \mathbf{B} , respectively), the adiabatic index γ , the simulation time t , and the number of zones.

Test	State	ρ	p_g	v_x	v_y	v_z	B_x	B_y	B_z	γ	t	Zones
CW1	L	10.0	1.0	0.0	0.7	0.2	5.0	1.0	0.5	5/3	1.0	40
	R	1.0	1.0	0.0	0.7	0.2	5.0	1.0	0.5			
CW2	L	1.0	1.0	0.2	0.0	0.0	1.0	1.0	0.0	5/3	1.0	40
	R	0.125	1.0	0.2	0.0	0.0	1.0	1.0	0.0			
RW	L	1.0	1.0	0.4	-0.3	0.5	2.4	1.0	-1.6	5/3	1.0	40
	R	1.0	1.0	0.377237	-0.482389	0.424190	2.4	-0.1	-2.178213			
ST1	L	1.0	1.0	0.0	0.0	0.0	0.5	1.0	0.0	2.0	0.4	400
	R	0.125	0.1	0.0	0.0	0.0	0.5	-1.0	0.0			
ST1-B0	L	1.0	1.0	0.0	0.0	0.0	0.0	1.0	0.0	2.0	0.4	400
	R	0.125	0.1	0.0	0.0	0.0	0.0	-1.0	0.0			
ST2	L	1.08	0.95	0.4	0.3	0.2	2.0	0.3	0.3	5/3	0.55	800
	R	1.0	1.0	-0.45	-0.2	0.2	2.0	-0.7	0.5			
ST3	L	1.0	0.1	0.999	0.0	0.0	10.0	7.0	7.0	5/3	0.4	400
	R	1.0	0.1	-0.999	0.0	0.0	10.0	-7.0	-7.0			
ST4	L	1.0	5.0	0.0	0.3	0.4	1.0	6.0	2.0	5/3	0.5	800
	R	0.9	5.3	0.0	0.0	0.0	1.0	5.0	2.0			
ST5	L	1.0	30.0	0.0	0.0	0.0	5.0	6.0	6.0	5/3	0.4	800
	R	1.0	1.0	0.0	0.0	0.0	5.0	0.7	0.7			

Table 2. Mean ratios of CPU running time between the HLLC solver and the HLL solver, $t_{\text{hllc}}/t_{\text{hll}}$. To compute the mean ratios in 1D tests (ST1 to ST5), we first measure the ratio of CPU running times for each of the working resolutions employed in this paper, $t_{\text{hllc}}/t_{\text{hll}}(n_{x,i})$, $n_{x,i} = \{50, 100, 200, 400, 800, 1600, 3200\}$, and then average over all of these results (i.e., $t_{\text{hllc}}/t_{\text{hll}} \text{xs} := \frac{1}{7} \sum_{i=1}^7 t_{\text{hllc}}/t_{\text{hll}}(n_{x,i})$). Likewise, for the 2D tests (RR and CE) the average of ratios of CPU time is computed performing them with resolutions of 50×50 , 100×100 , 200×200 and 400×400 .

CPU running times								
test	ST1	ST1-B0	ST2	ST3	ST4	ST5	RR	CE
$t_{\text{hllc}}/t_{\text{hll}}$	1.06	1.06	1.06	1.13	1.18	1.15	1.05	1.18

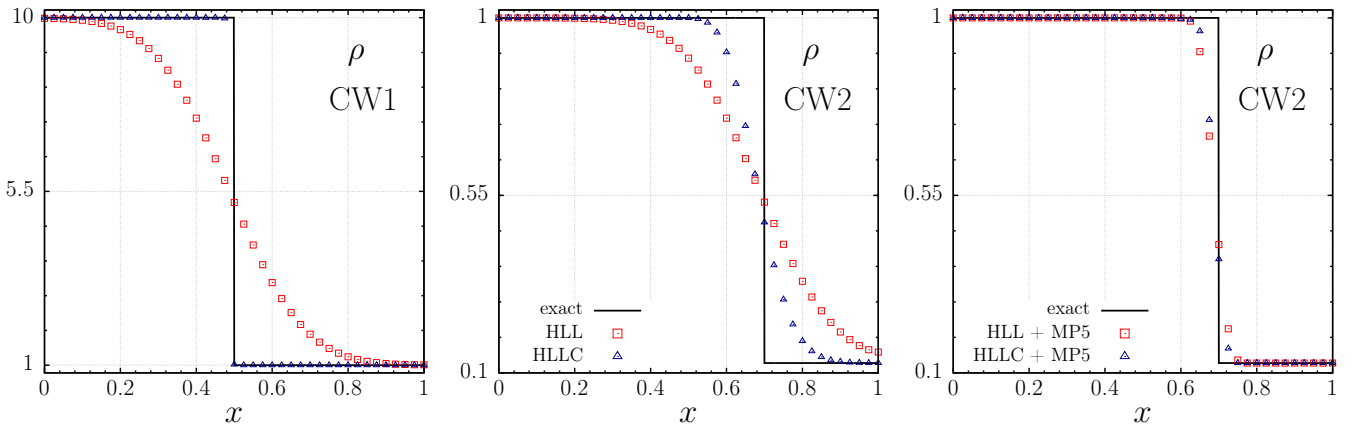


Figure 1. **CW:** Rest-mass density at $t = 1.0$ in contact wave discontinuity tests CW1 (left panel) and CW2 (central and right panels; see Tab. 1) performed with the HLL (red squares) and the HLLC (blue triangles) approximate Riemann solvers. The analytical solution is depicted with a black solid line. In the simulation presented in the right panel, the MP5 scheme is used, whereas in the other simulations the piecewise constant reconstruction (Godunov) is employed.

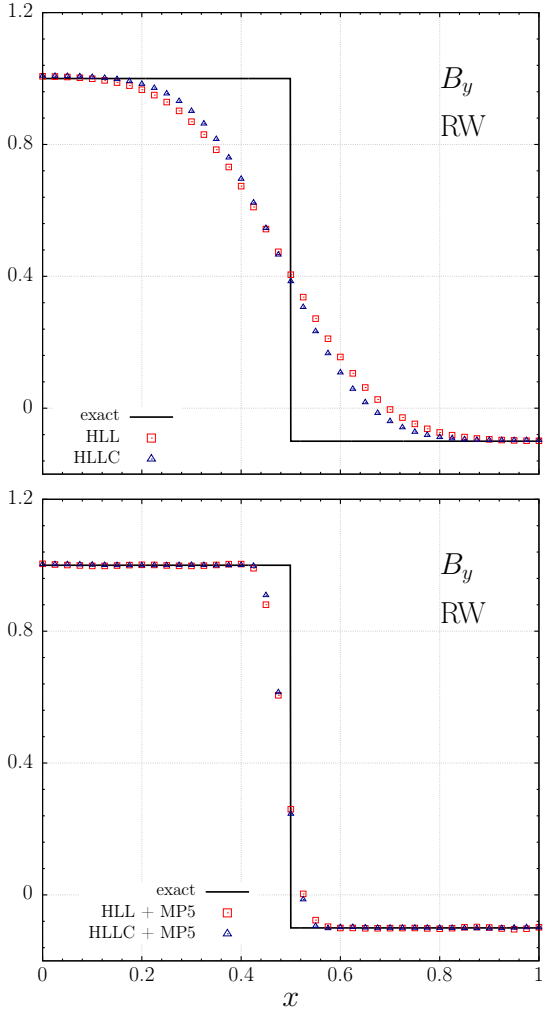


Figure 2. RW: Magnetic field (B_y component) for an isolate rotational wave at $t = 1$. The solid line stands for the analytic solution, blue triangles and red squares symbols show the solution with the HLLC and HLL solvers, respectively. The upper panel is computed without employing any high-order intercell reconstruction (Godunov), while the lower panel corresponds to the same test using the MP5 reconstruction.

The initial discontinuity breaks into a left-going fast rarefaction, a left-going compound wave, a contact discontinuity, a right-going slow shock and a right-going fast rarefaction wave (Fig. 3). According to the analytic solution (Giacomazzo & Rezzolla 2006)⁴, the contact discontinuity must be located at $x \approx 0.6$. The structure of the contact is more accurately resolved by the HLLC solver than by the HLL solver as can be seen in the zoomed Fig. 4.

Both solvers are slightly more diffusive in this test than their ideal RMHD counterparts (compare our Fig. 4 to, e.g., Fig. 4 of Mignone et al. (2009) or to Fig. 4 of Antón et al. (2010), where the test is shown with the same resolution).

⁴ Giacomazzo & Rezzolla (2006) solution is built explicitly neglecting compound waves. Besides their physical or unphysical nature, numerically the compound wave shows up at $x \simeq 0.5$, inducing the seemingly large deviation of the numerical solution from the analytic one in the vicinity of its location.

This extra diffusivity comes from two sources. First, our estimates for the limiting speeds of the approximate Riemann solvers ($\lambda_r = +1$, $\lambda_l = -1$; Sec. 4) are larger in absolute value than the fast magnetosonic waves for this test in ideal RMHD. The latter are commonly employed as estimators of the fastest signal speeds in HLL and HLLC approximate Riemann solvers for RMHD. Note, however, that fast-magnetosonic waves propagate at the speed of light in RRMHD. Second, the notorious degeneracy of the eigenfields limiting the Riemann fan (Eq. 15) increases the amount of numerical dissipation added to characteristic variables corresponding to eigenvalues without jumps for certain electromagnetic configurations.

To quantify the accuracy of the HLL and HLLC solvers, we use the discrete L1-norm error, in the form:

$$\varepsilon_{\text{L1}} = \frac{1}{n_x} \sum_{i=1}^{n_x} |U_i^{\text{ref}} - U_i|, \quad (50)$$

where U_i^{ref} is a reference solution computed with the exact solver of Giacomazzo & Rezzolla (2006) on the same grid as the numerical solution U_i . n_x is the number of numerical grid zones in the x -direction. For the 1D tests, we evaluate the L1-norm errors of the B_y component of the magnetic field and display them as a function of the number of numerical zones in Fig. 5.

The measured errors for the ST1 test are $\sim 20\%$ smaller using the HLLC solver than using the HLL solver for $n_x > 100$ (Fig. 5, top left panel), reflecting that the HLLC solutions are closer to the exact ones than the HLL numerical approximations.

Differently from the ideal RMHD implementation of the HLLC solver by Mignone & Bodo (2006), our approximate Riemann solver does not need to distinguish between the cases $B_x = 0$ and $B_x \neq 0$ (see Sec. 4). To demonstrate this, we consider the ST1-B0 test (see Tab. 1) which is like the ST1 test, but with $B_x = 0$. The structure of the solution to this test only contains two fast waves, a rarefaction moving to the left and a shock moving to the right with a tangential discontinuity between them. In contrast to the standard ST1 test, compound waves are not present in ST1-B0. The new HLLC solver can deal with this setup at the same quantitative level as in the case with $B_x \neq 0$ (Fig. 6). A small overshooting in the thermal pressure across the tangential discontinuity (at $x \simeq 0.63$) is present in both approximate Riemann solvers, but the contact wave is more sharply resolved with the HLLC than with the HLL solver (Fig. 7).

Discrete L1-norm errors of the magnetic field B_y component, computed for the ST1-B0 test, are plotted in the upper mid panel of Fig. 5. In this case the difference between L1-norm errors for the HLL and HLLC solvers reduces substantially as compared to the ST1 test. This happens because the jump across the contact wave is zero in this test and, as a result, the potential advantage of the HLLC solver with respect to the HLL solver drastically reduces. Anyway, the HLLC L1-norm errors are a bit smaller than the corresponding HLL L1-norm errors at all resolutions. We observe that the computational overhead of the HLLC solver with respect to the HLL solver is very modest (Tab. 2). On average, employing the former solver takes only $\sim 6\%$ more time to compute the solution in the ST1 and ST1-B0 tests.

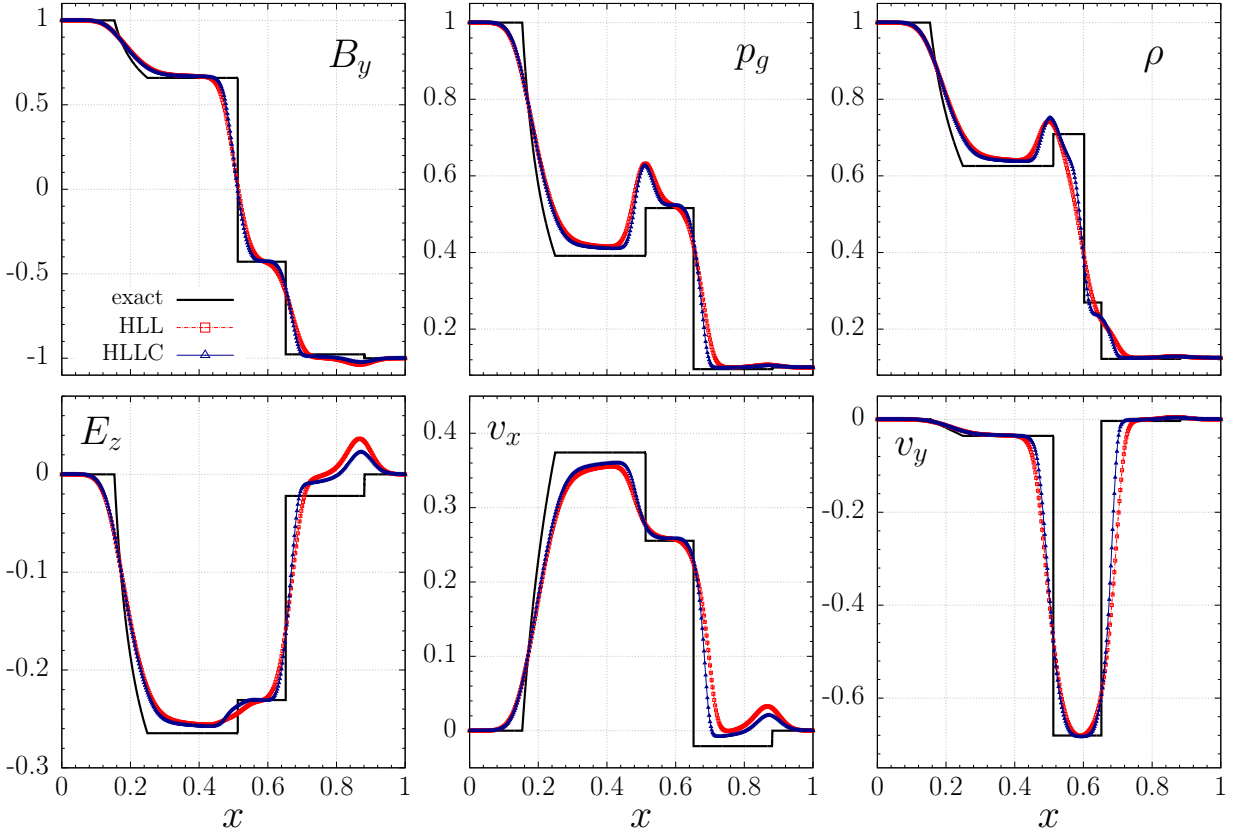


Figure 3. ST1: Relativistic Brio-Wu shock tube test at $t=0.4$. The calculations are performed with a 1st-order accurate scheme on a grid of 400 zones employing the HLL (red symbols) and HLLC (blue symbols) Riemann solvers. The analytic solution of this test in ideal RMHD is displayed with black solid line. Upper panel: magnetic field (B_y component), thermal pressure (p), rest-mass density (ρ). Lower panel: electric field (E_z component), velocity field (v_x and v_y components).

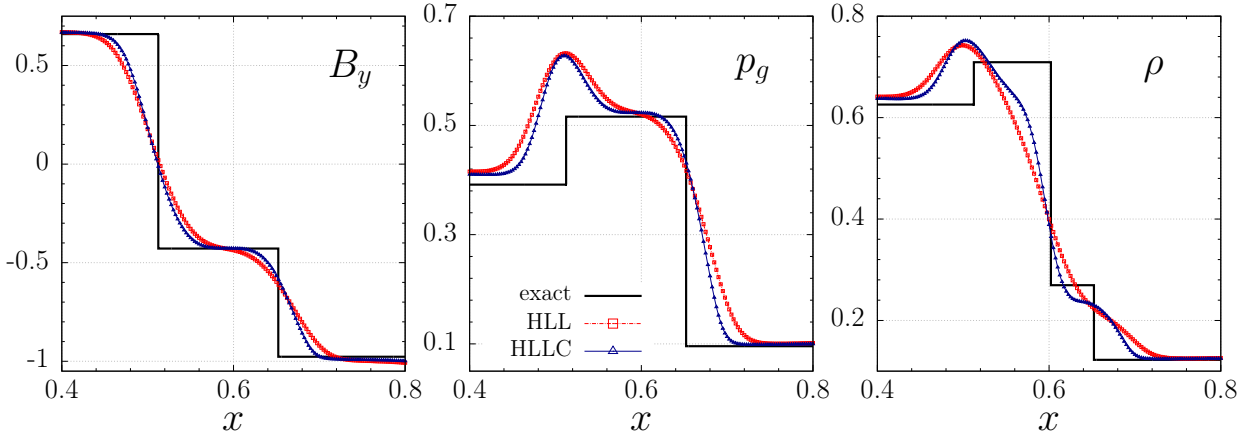


Figure 4. ST1: Zoom of Fig. 3 on the region where the contact discontinuity is located. From left to right: magnetic field (B_y component), thermal pressure (p_g) and rest-mass density (ρ).

5.4 Shock Tube Problem 2 (ST2)

In this shock tube problem, the break up of the initial discontinuity develops a Riemann fan with 7 different waves in the ideal limit. We use the same set up as Antón et al. (2010) (in RMHD) or as Dumbser & Zanotti (2009) or Bucciantini & Del Zanna (2013) in RRMHD, where the computational domain, $x \in [0, 1]$, is resolved with a uniform grid of 400 cells and the test is evolved until a final

time $t = 0.55$. The HLLC solver attains a sharper representation of the entropy wave located at $x \simeq 0.48$ than the HLL solver (Fig. 8). Nonetheless, an undershooting ahead of the entropy wave is evident in the HLLC solution. The state between the right-going slow shock ($x \simeq 0.7$) and the right-going Alfvén wave at $x \simeq 0.73$ is smeared by both solvers albeit the HLLC solution is slightly closer to the analytical one also in that region (Fig. 9). It is also the case for the

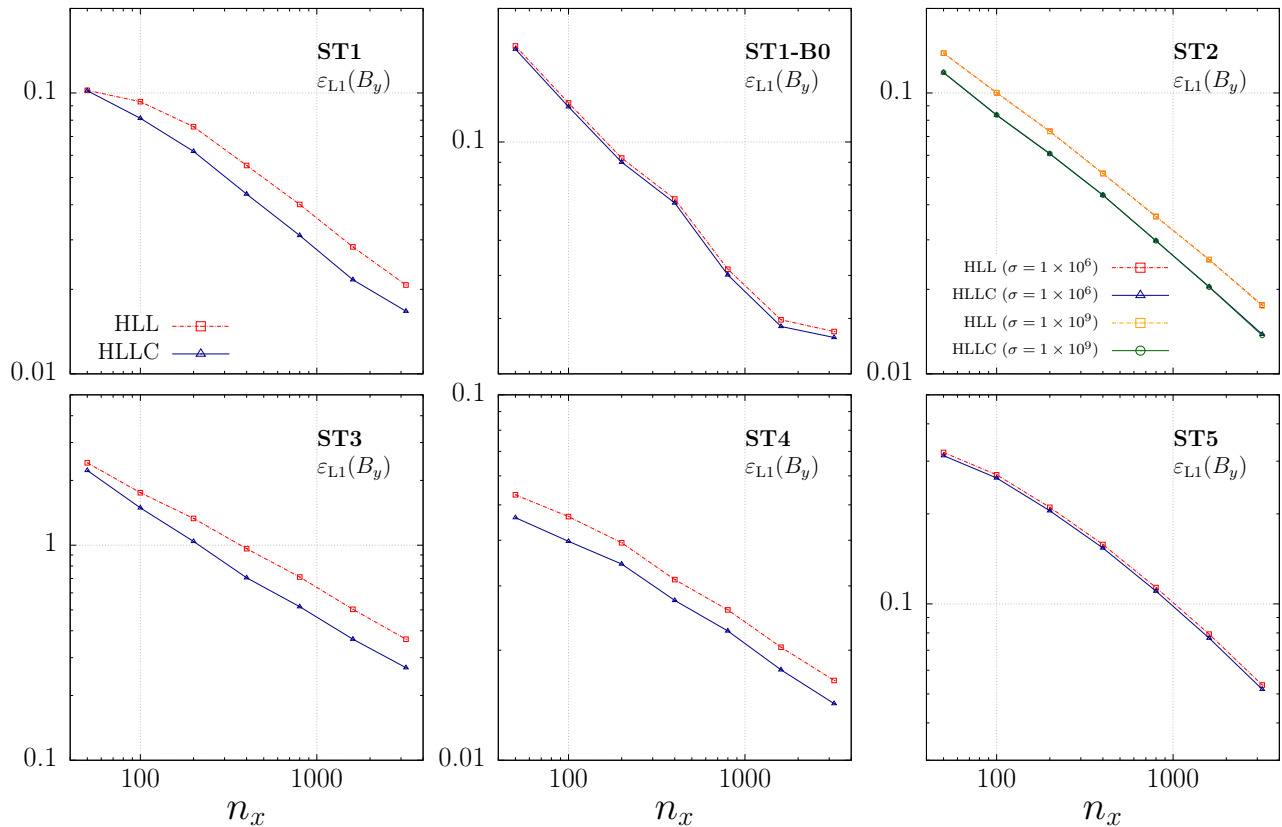


Figure 5. L1-norm errors (Eq. 50) of B_y magnetic field component in six shock tube problems presented in Tab. 1. All tests were performed with resolutions of $n_x = 50, 100, 200, 400, 800, 1600, 3200$ grid zones, and a small $C_{\text{CFL}} = 0.1$ to avoid contributions to the error arising from the time discretisation. The numerical solutions computed with the HLL and HLLC solvers are displayed with red and blue squares, respectively.

state between the left-going Alfvén wave ($x \simeq 0.185$) and the left going slow rarefaction at $x \simeq 0.19$. In the latter case, the two waves are so close to each other that none of the approximate Riemann solvers can resolve them. Indeed, this is to be expected, since resolving this region is a challenge even for the exact solver of Giacomazzo & Rezzolla (2006), which cannot obtain a solution for this test with an accuracy better than 3.4×10^{-4} .

The L1-norm errors in this test (Fig. 5 upper right panel) show again a larger accuracy of the solutions computed with the HLLC solver. These errors are $\sim 10\%$ lower than for equivalent tests performed with the HLL solver, almost independently of the resolution employed. Remarkably, for the ST2 test, the computational cost to obtain the solution employing the HLLC solver is only a $\sim 6\%$ larger than using the HLL solver (Tab. 2).

In Fig. 10, we explore the dependence of the results on the conductivity σ analogously to the studies done by Dumbser & Zanotti (2009) and Bucciantini & Del Zanna (2013). Resistive versions of the shock tube problem ST2 display smoother profiles of B_y with decreasing conductivity. Noteworthy, the cases with $\sigma = 10^9$ and 10^6 basically overlap at a resolution of $n_x = 800$ zones. From this fact, we draw two conclusions. First, since the results basically are insensitive to the exact value of the conductivity, when it is large enough, we can assess that for $\sigma \gtrsim 10^6$ the numerical resistivity is larger than the physical one in this particular

set up. Second, the *proximity* of the results to the analytic solution justifies our choice of $\sigma = 10^6$ as a conductivity value close enough to the ideal RMHD limit. This result is expressed more quantitatively in Fig. 5 (upper right panel; orange and green lines). For both solvers, the L1-norm errors are basically the same in tests set up with $\sigma = 10^6$ and $\sigma = 10^9$.

5.5 Shock Tube Problem 3 (ST3)

In this test, two relativistic, magnetised streams collide producing two “reverse” strong relativistic fast shocks propagating symmetrically from the mid point of the computational domain (see, e.g., Balsara 2001; Del Zanna et al. 2003; Leismann et al. 2005; Mignone & Bodo 2006; Mignone et al. 2009; Antón et al. 2010). Following the fast shocks, a pair of symmetric slow shocks further thermalise the plasma in the state delimited by them, converting all the remaining kinetic energy into thermal energy and leaving the fluid at rest (Fig. 11). In this test there is not a jump of the variables across the contact wave (standing at $x = 0$) and, therefore, the differences between HLL and HLLC are rather small. However, the HLLC approximate Riemann solver produces a slightly sharper representation of the intermediate discontinuities (slow shocks).

Even though both solvers display a pathological undershooting of the density at the grid center, the den-

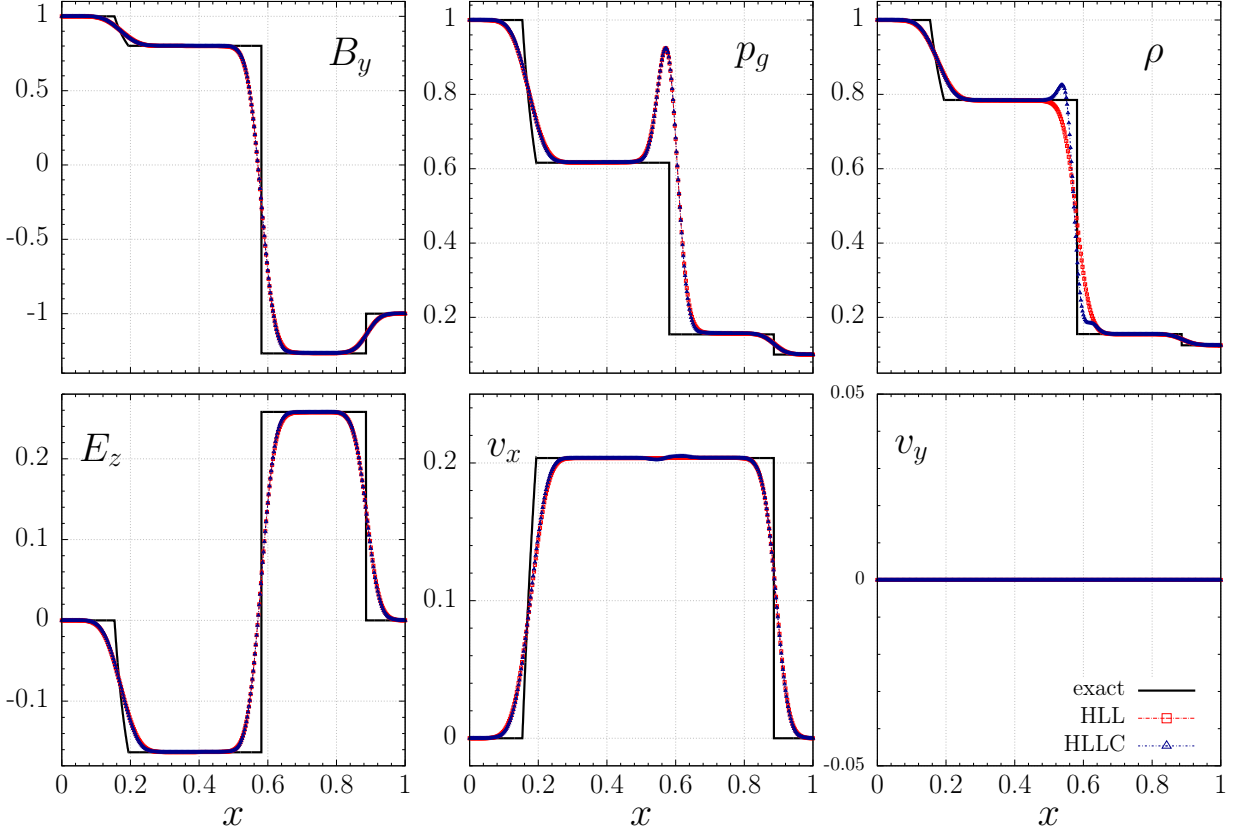


Figure 6. ST1-B0: Variant of the Relativistic Brio-Wu shock tube test at $t=0.4$ when the longitudinal magnetic field is zero ($B_x = 0$). The panels, lines and symbols are the same as in Fig. 3.

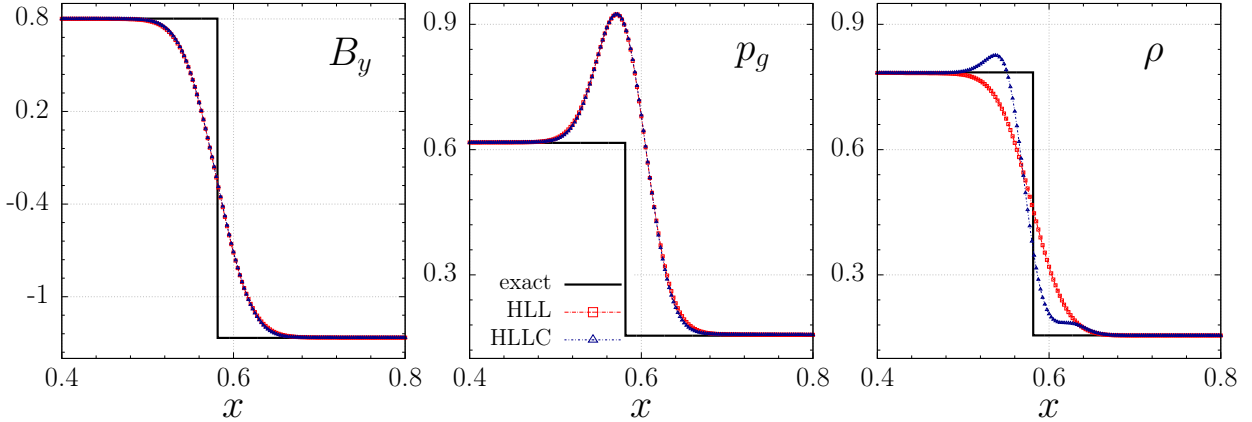


Figure 7. ST1-B0: Same as Fig. 4 but for test ST1-B0.

sity decrease for the HLLC solver is substantially larger than for the HLL solver. This is a well known pathology of many Godunov-type schemes known as “wall heating” problem (Noh 1987), which is more stringent for approximate solvers possessing smaller numerical dissipation. Hence, the HLL solver displays a much smaller undershooting than the HLLC solver at $x = 0.5$ (Fig. 12). The slightly higher quality of the HLLC solution is quantified by the smaller L1-norm errors obtained with the latter solver in comparison to the HLL solver (Fig. 5 bottom left panel). At the maximum resolution employed ($n_x = 3200$) the errors made with the

HLLC solver are $\sim 26\%$ smaller than the ones made with the HLL solver. For the ST3 test, the computational cost to obtain the solution employing the HLLC solver is $\sim 13\%$ larger than using the HLL solver (see Tab. 2).

5.6 Shock Tube Problem 4 (ST4)

Giacomazzo & Rezzolla (2006) refer to this Riemann problem as “Generic Alfvén” test, which is very challenging for ideal RMHD as well as RRMHD codes, as it encompasses all seven possible waves in the Riemann fan it develops. It

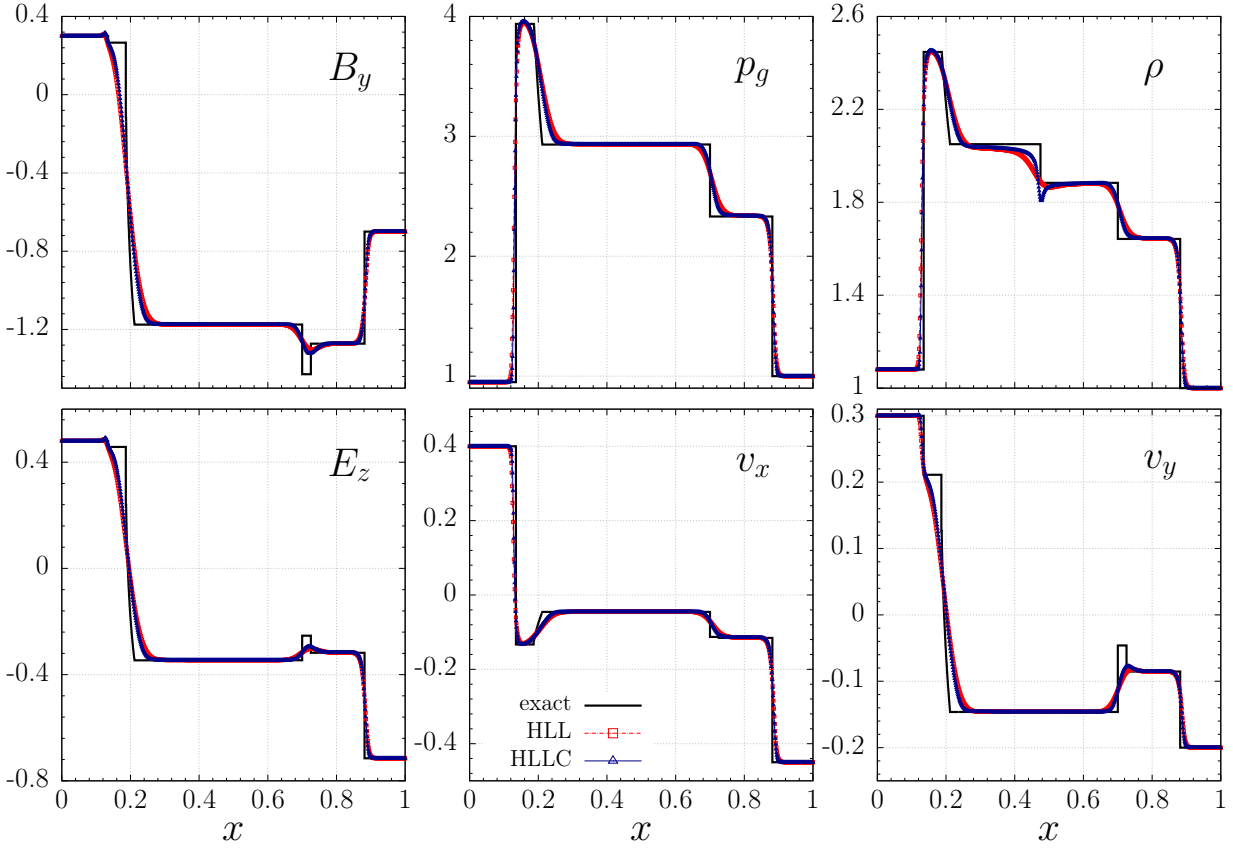


Figure 8. ST2: Second 1D Riemann problem (Tab. 1) after $t = 0.55$ and using 400 numerical zones. The variables displayed and the meaning of the symbols and lines is the same than in Fig. 3.

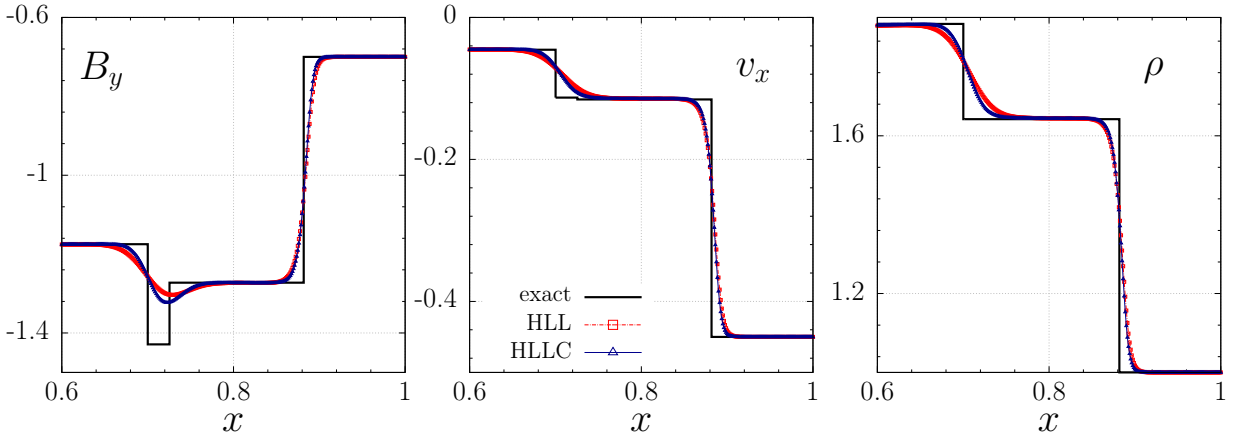


Figure 9. ST2: Zoom of some of the variables displayed in Fig. 8 focusing on the right-going slow shock ($x \approx 0.7$), Alfvén wave ($x \approx 0.73$) and fast shock ($x \approx 0.88$). From left to right: magnetic field (B_y component), velocity (v_x component) and rest-mass density (ρ).

has been adopted as a benchmark by, e.g., [Mignone et al. \(2009\)](#) and [Antón et al. \(2010\)](#). For this setup, the initial discontinuity results into a contact discontinuity which separates a fast rarefaction wave (at $x \approx 0.05$), a rotational wave (at $x \approx 0.44$), and a slow shock (at $x \approx 0.46$), from a slow shock (at $x \approx 0.56$), an Alfvén wave (at $x \approx 0.57$) and a fast shock (at $x \approx 0.97$). The exact solution of this test, together with the results at $t = 0.4$ for the HLLC and HLL solvers, are shown in Fig. 13. The finest structures in this test, associated with the rotational discontinuities trav-

elling very close to the slow shocks, are hardly resolved by the 1st-order scheme using any of the approximate Riemann solvers employed in this paper at the working resolution of 800 uniform numerical zones (Fig. 14).

The L1-norm errors of this test (Fig. 5 bottom mid panel) show the same qualitative trend than those of the ST2 test (Fig. 5 upper right panel). The HLLC numerical solution yields L1-norm errors $\sim 13\%$ smaller than the HLLC counterpart almost independently of the numerical resolution. For the ST4 test, the computational cost to obtain the solu-

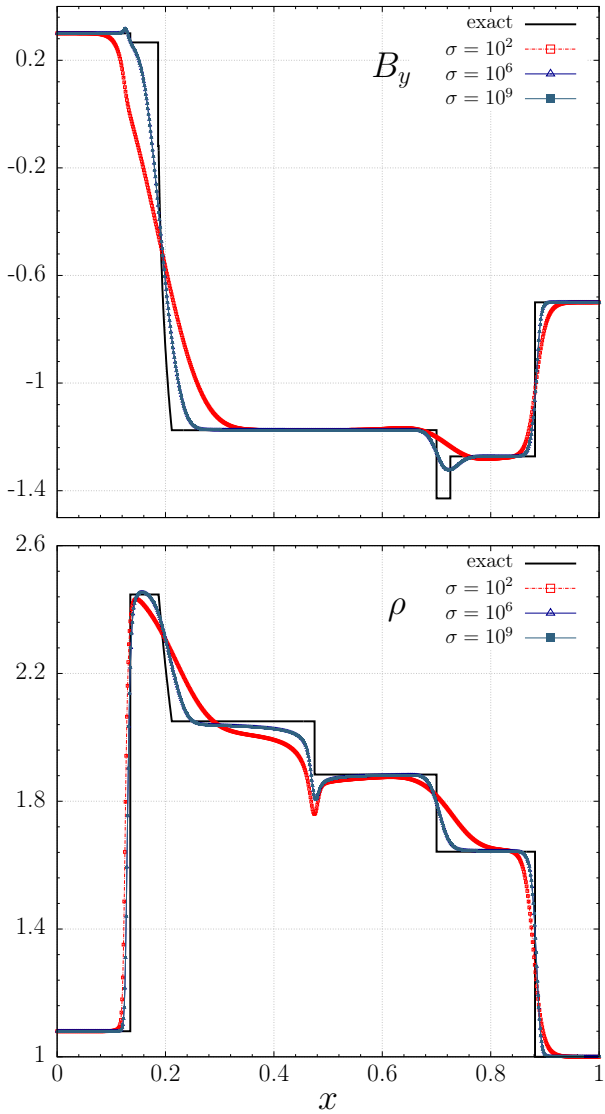


Figure 10. ST2-resistive: Results of the second 1D Riemann problem (ST2; Tab. 1) after $t = 0.55$ and using 800 numerical zones, but for different conductivities $\sigma = 10^9, 10^6, 10^2$ and the HLLC solver. Note that the lines and symbols corresponding to the case $\sigma = 10^9$ overlap with the case $\sigma = 10^6$.

tion employing the HLLC solver is $\sim 18\%$ larger than using the HLL solver (Tab. 2). This represents the largest computational overhead of all the 1D tests presented in this section. The larger computing time is explained in terms of the challenging nature of the ST4 test, that develops several regions where very fine structures are attempted to be resolved by the HLLC solver (while they are completely smeared out by the HLL solver).

5.7 Shock Tube Problem 5 (ST5)

The relativistic blast wave test problem with a moderate initial pressure difference was proposed by (Balsara 2001). The Riemann problem develops a left-going fast rarefaction wave (at $x \simeq 0.16$) and slow rarefaction fan (at $x \simeq 0.53$) are separated by a contact discontinuity (at $x \simeq 0.76$) from

two right-going shock waves, a slow (at $x \simeq 0.86$) and fast (at $x \simeq 0.9$) one. The overall structure of the solution can be found in Fig. 15, where it is evident the inability of either HLLC or HLL to properly capture the finest structure left to the right-going slow shock wave. The contact wave is slightly better resolved with the HLLC solver than with the HLL solver, as can be seen in Fig. 16. The marginally better performance of the HLLC solver at all the resolutions considered is quantified in terms of the L1-norm errors of the rest-mass density (Fig. 5 bottom right panel). The proximity of the L1-norm errors obtained with the HLLC and HLL solver is due to the fact that the contact discontinuity in this test is moving faster than in any other 1D tests shown in this section. This reduces the sharpness with which the contact wave is captured by the HLLC scheme, as discussed for the CW2 test in Sec. 5.1.

Finally, we have measured a mean computational overhead of $\sim 15\%$ using the HLLC solver in the ST5 test with respect to the corresponding models employing the HLL solver (Tab. 2).

5.8 Resistive rotor (RR)

The resistive rotor (see, e.g., Dumbser & Zanotti 2009; Bucciantini & Del Zanna 2013) is of interest not only as a calibration test for resistive as well as ideal MHD numerical multidimensional codes, but also because of its connection to the problem of angular momentum loss through torsional Alfvén waves in star formation (Mouschovias & Paleologou 1980). It consists of an initial 2D state where in a region of radius $r \leq 0.1$ around the domain center, the density is $\rho = 10$, and the fluid rotates with constant angular velocity $\Omega = 8.5$. Outside this region ($r > 0.1$) the medium at rest is uniform ($\rho = 1$). Both the pressure ($p_g = 1$) and the magnetic field $\mathbf{B} = (1, 0, 0)$ are uniform in the whole computational domain, a unit square covering the range $-0.5 \leq x \leq 0.5$, $-0.5 \leq y \leq 0.5$. The initial electric field is set like in ideal RMHD, and the adiabatic index is $\gamma = 4/3$. Figure 17 shows snapshots of the gas pressure p and of the electric field component E_z at $t = 0.3$, in different conductivity regimes (cases with $\sigma = 10^6, 10^3$ and 10 are considered). The model was obtained using the second order MIRK scheme, the MP5 intercell reconstruction, with a CFL factor $C_{\text{CFL}} = 0.1$, the HLLC approximate Riemann solver and a grid of 300 zones per dimension.

Our results agree relatively well with those of Dumbser & Zanotti (2009) and Bucciantini & Del Zanna (2013) for intermediate ($\sigma = 10^3$) or almost ideal ($\sigma = 10^6$) regimes. In the resistive regime ($\sigma = 10$), the differences are more obvious though. The interface between the high-density, rotating central cylinder and the external medium develops small amplitude instabilities in our case (visible in the upper right panel of Fig. 17). Also the two dimensional distribution of E_z (Fig. 17 lower right panel) *seems* more circularly symmetric in our case. We note, however that the vertical scale of Bucciantini & Del Zanna (2013) is compressed with respect to the horizontal one in their Fig. 3. Hence all the structures look more oblate than what they actually are in our figures, where the vertical and horizontal scales are isotropic. The differences between our approach and those of Dumbser & Zanotti (2009) and Bucciantini & Del Zanna (2013) likely stem from the

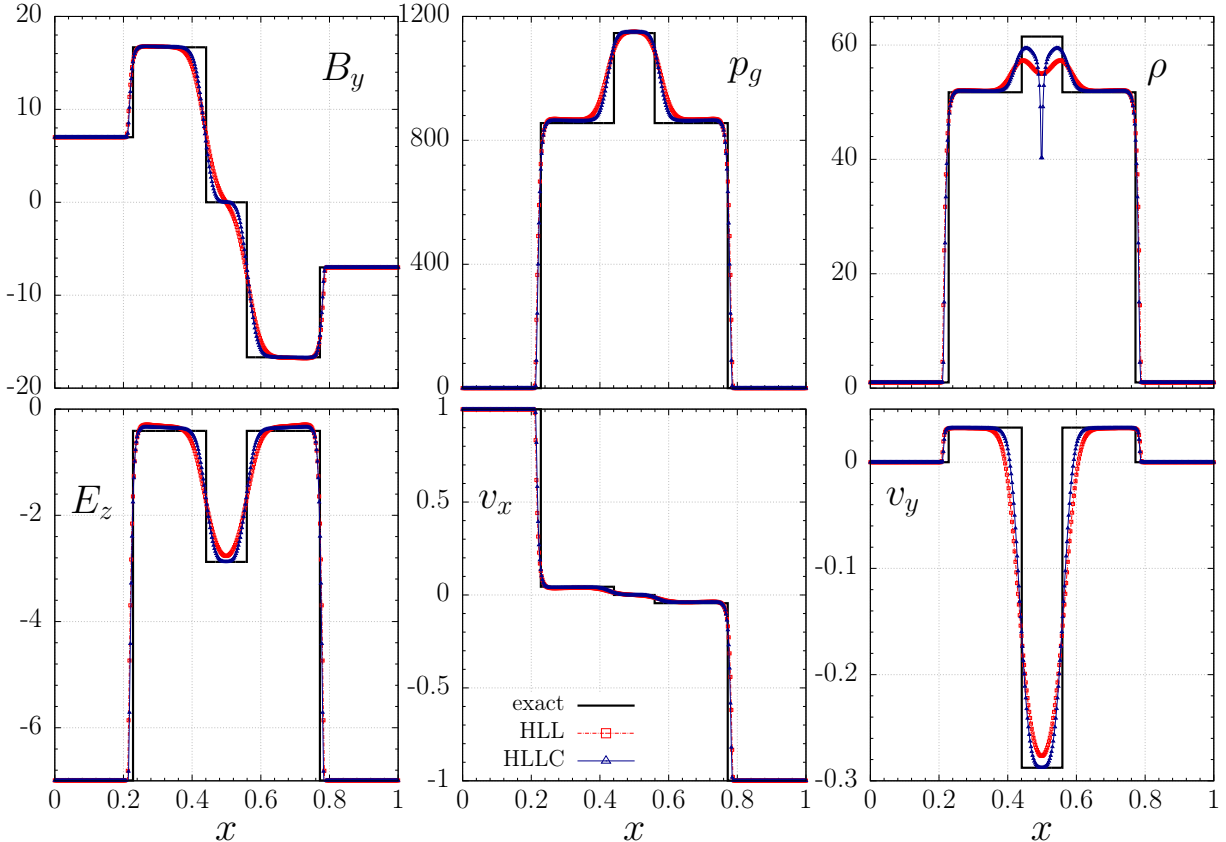


Figure 11. ST3: Collision of two oppositely moving streams of plasma after $t = 0.4$ computed with 400 numerical zones. Upper panels (from left to right): magnetic field (B_y component), thermal pressure (p_g), rest-mass density (ρ). Lower panels (from left to right): electric field (E_z component), velocity (v_x and v_y components).

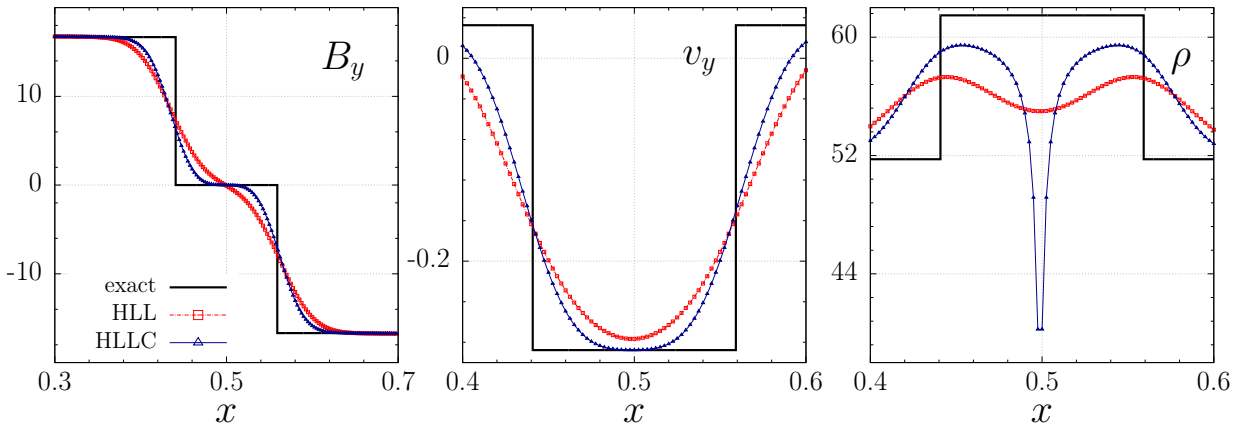


Figure 12. ST3: Magnification of the central region of the ST3 test encompassing the two slow shocks located at $x \simeq 0.44$ and $x \simeq 0.56$. From left to right: magnetic field (B_y component), velocity (v_y component) and rest-mass density (ρ).

distinct numerical methodologies employed. For instance, Bucciantini & Del Zanna (2013) employ a *fully constrained* scheme, i.e., they do not have an explicit equation for the charge conservation as we do, but instead impose $\nabla \cdot \mathbf{E} = q$. Furthermore, they enforce the magnetic solenoidal constraint, $\nabla \cdot \mathbf{B} = 0$ employing staggered grids via the upwind constrained transport method (Del Zanna et al. 2003), while we resort to the hyperbolic divergence cleaning method of Dedner et al. (2002). However, we find that the spatial re-

construction is one of the most relevant differences to explain the discrepancies in the low- σ regime. In such a resistive regime the wave structure changes drastically, with a faster expanding electric field, which is no longer inductive (see also the transverse profile of the solution along the $x = 0$ axis in Fig. 18 lower panels). We have employed the 5th-order accurate reconstruction scheme MP5, while Bucciantini & Del Zanna (2013) resort to a 3rd-order accurate Central Essentially Non-Oscillatory spatial reconstruc-

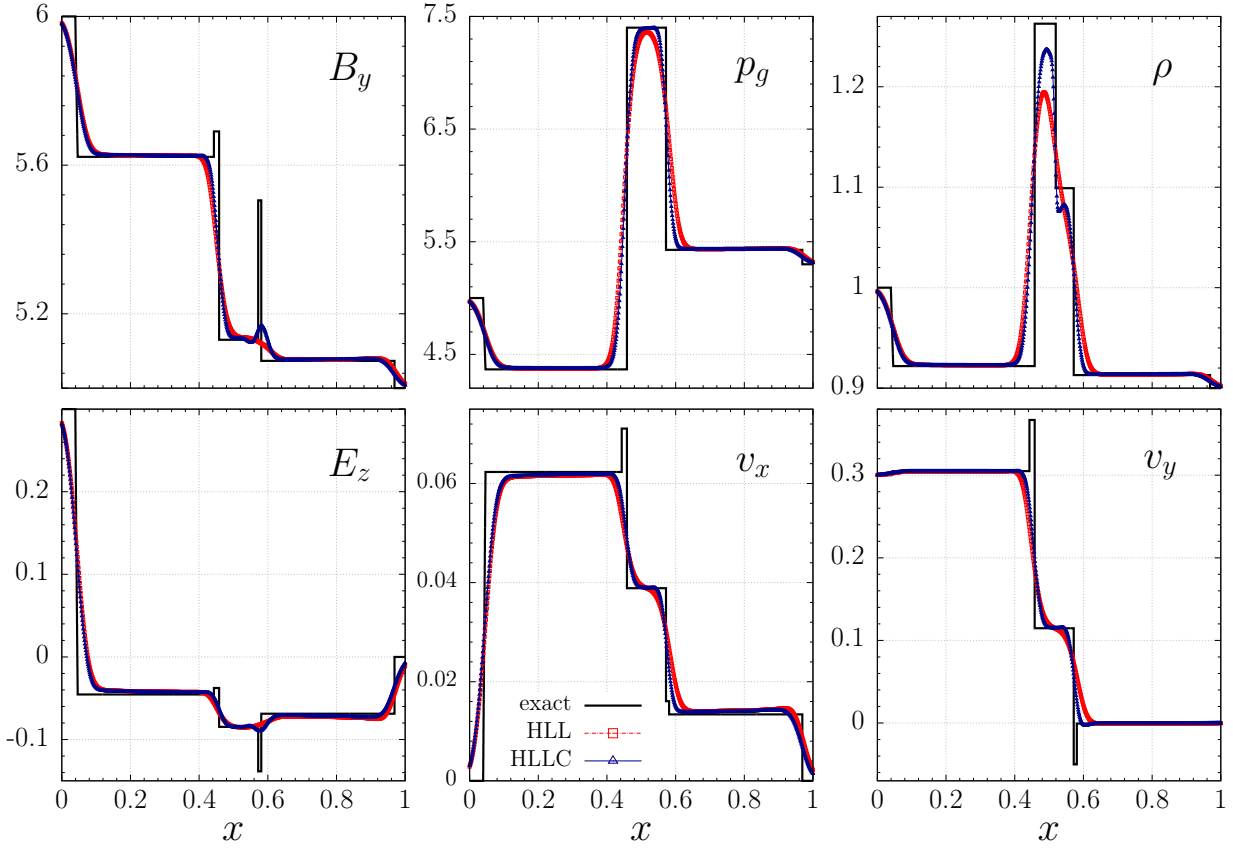


Figure 13. ST4: Numerical results for the generic Alfvén test problem ST4, after $t = 0.4$ on a grid with 800 numerical zones. Upper panels (from left to right): magnetic field (B_y component), thermal pressure (p_g), rest-mass density (ρ). Lower panels (from left to right): electric field (E_z component), velocity (v_x and v_y components).

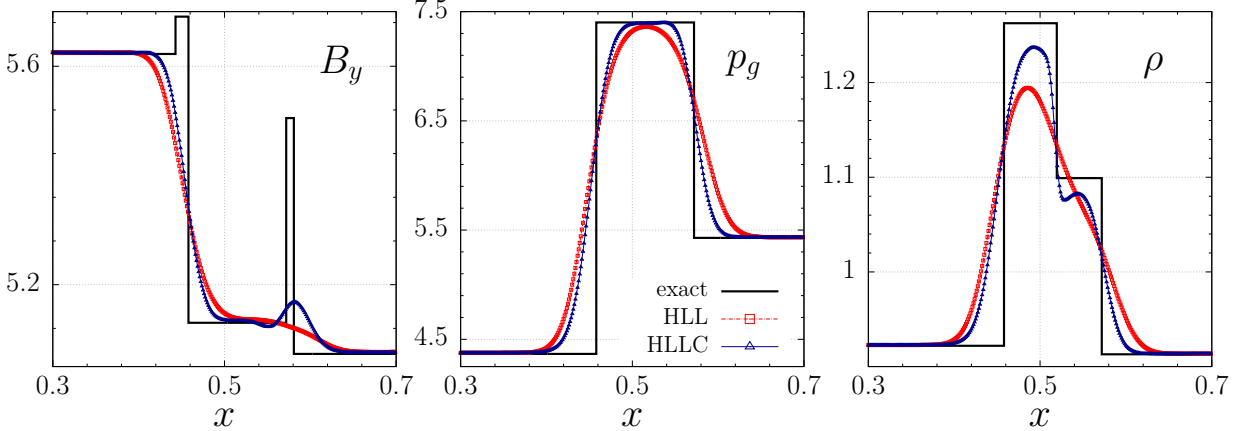


Figure 14. ST4: Enlargement of the central region of Fig. 13. From left to right: magnetic field (B_y component), thermal pressure (p_g) and rest-mass density (ρ).

tion with a Monotonised Center (MC) limiter. We have repeated the resistive rotor test reducing the order of the spatial reconstruction. For that we have employed a 2nd-order MC intercell reconstruction, finding that the differences with respect to Bucciantini & Del Zanna (2013) for the case $\sigma = 10$ are significantly reduced. We especially observe a reduction of the perturbations in the pressure at the transition layer between the central, rotating cylinder and the initially static outer medium. Our results hint

towards an excessive dissipation of the algorithms, both of Bucciantini & Del Zanna (2013) and of ours, for low-order spatial reconstructions. The differences in the resistive regime with respect to Dumbser & Zanotti (2009) can also be attributed to the usage of a lower order scheme (P_0P_2 in their case) compared to ours. Figure 18 shows a more quantitative comparison among the HLLC and HLL solvers with different spatial reconstructions. The smaller numerical resistivity of the HLLC solver stands out in the nearly-ideal

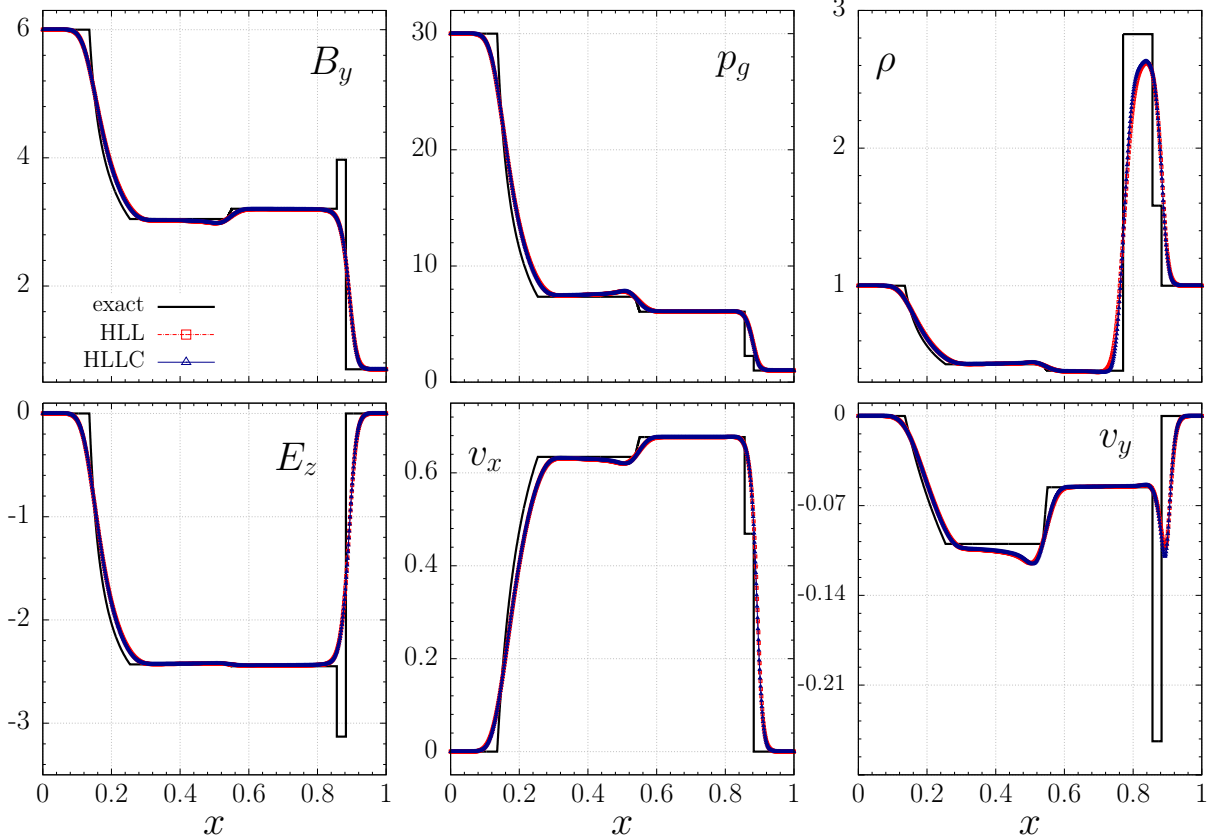


Figure 15. ST5: Numerical and exact solutions for the ST5 test at $t = 0.4$. Upper panel: magnetic field (B_y component), thermal pressure (p_g), rest-mass density (ρ). Lower panel: electric field (E_z component), velocity (v_x and v_y components).

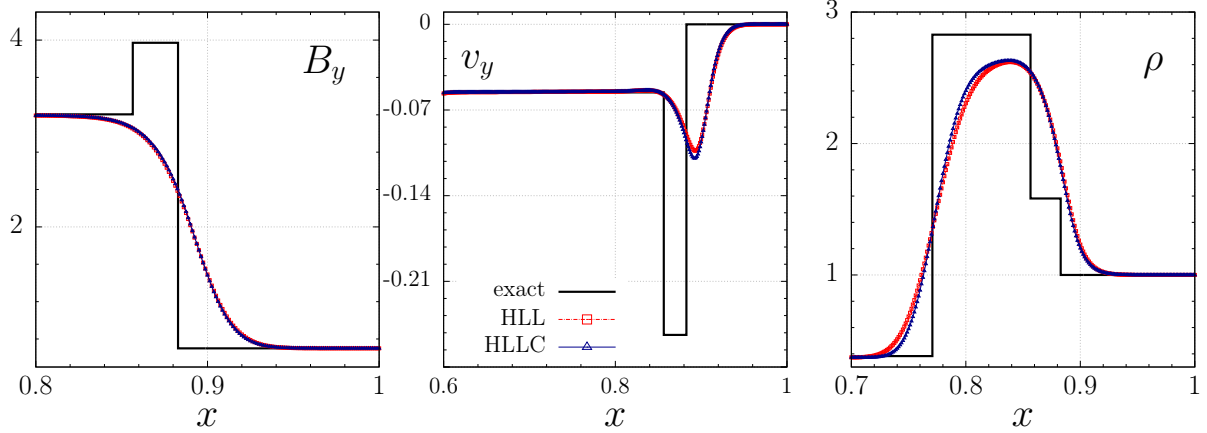


Figure 16. ST5: Magnification of a region of interest in Fig. 15. From left to right, magnetic field (B_y component), velocity (v_y) component and rest-mass density (ρ).

regime ($\sigma = 10^6$; Fig. 18 left panels) for tests with a 1st-order (Godunov) spatial reconstruction. The HLLC solver captures very well the sharp, small scale variations in the solution, which almost overlaps with that of models using the MP5 spatial reconstruction (compare the green line - HLLC- with the solutions using MP5 and either HLLC or HLL in the left panels of Fig. 18). At intermediate values of the conductivity ($\sigma = 10^3$) the solutions using the HLL and HLLC solvers are nearly overlapping, and the 1st-order schemes smear out the torsional Alfvén waves (small scale

structure) flanking the central core of the rotor (Fig. 18 central panels).

In this 2D test, the models run with the HLLC solver need $\sim 5\%$ larger computational time than those computed with the HLL solver.

5.9 Cylindrical Explosion (CE)

The cylindrical explosion test develops a strong shock propagating into a magnetically dominated medium. Results

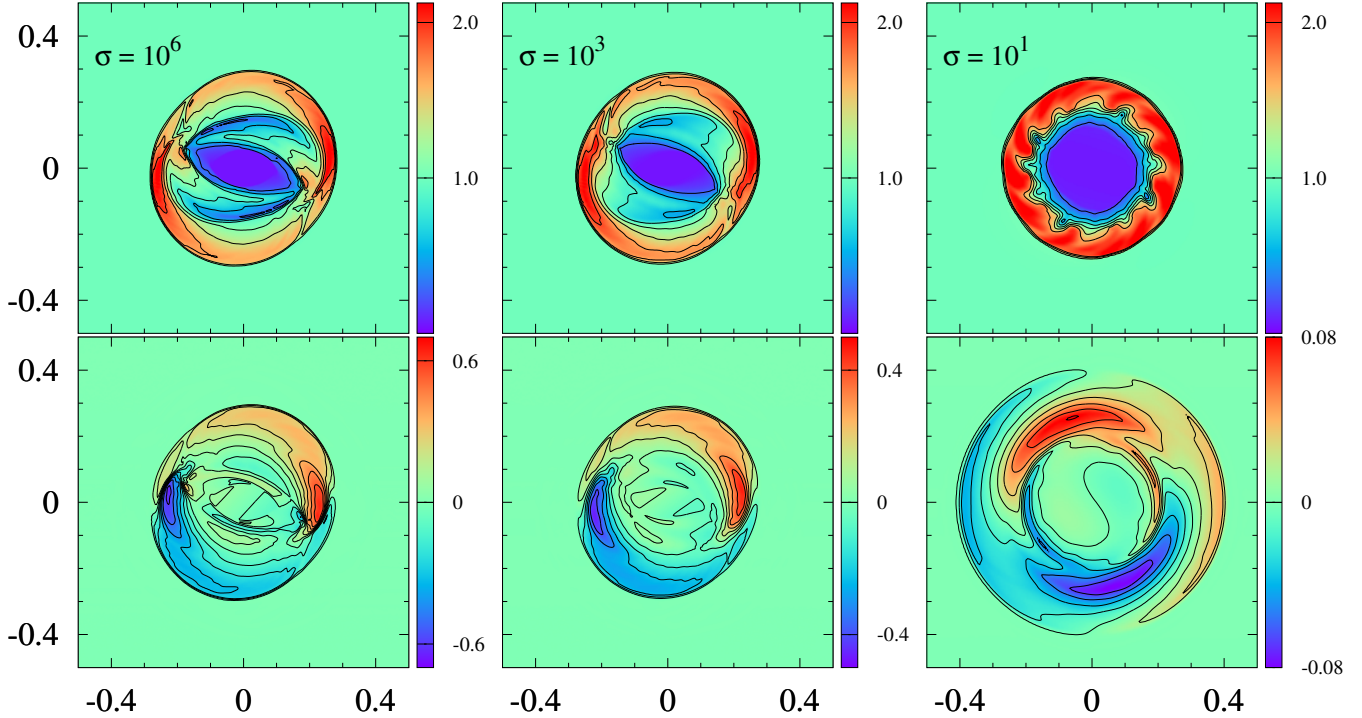


Figure 17. Resistive Rotor computed with a second order MIRK scheme, MP5 intercell reconstruction and a grid of 300×300 zones evolved up to a time $t = 0.3$. Upper panels: snapshots of the gas pressure. Lower panels: snapshots of E_z . We show the evolution for different values of the conductivity: the nearly ideal case $\sigma = 10^6$ (left panels), an intermediate or semi-resistive case $\sigma = 10^3$ (central panels) and a resistive case $\sigma = 10^1$ (right panels).

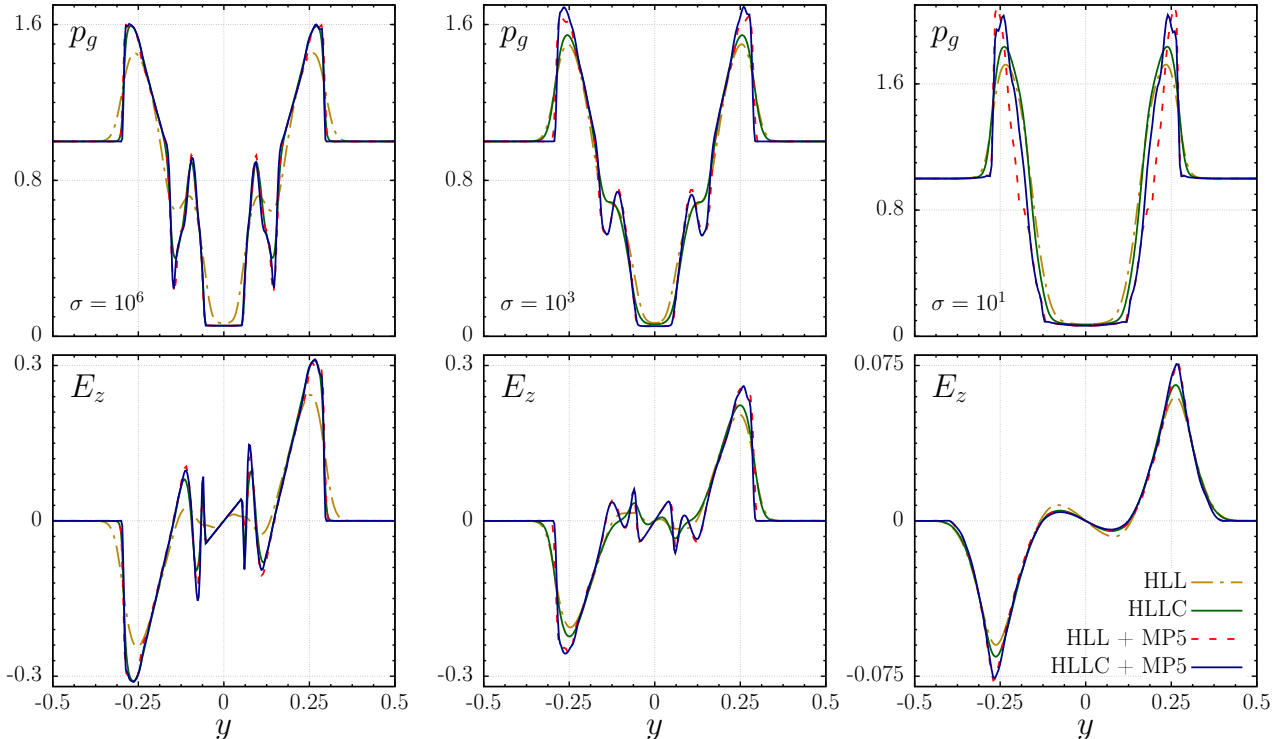


Figure 18. Profile along the $x = 0$ axis of the gas pressure (upper panels) and E_z (lower panels) for different values of the conductivity (labeled in each panel) at $t = 0.3$. Dash-dotted orange and solid green lines show the 1st-order schemes employing HLL and HLLC solvers, respectively. Dashed red and solid blue lines show the cases in which we combine the 5th-order intercell reconstruction (MP5) with either the HLL solver or the HLLC solver, respectively.

for different cylindrical explosion problems in RMHD (e.g., Komissarov 1999; Del Zanna et al. 2003; Leismann et al. 2005; Mignone & Bodo 2006; Martí 2015) as well as in the RRMHD regime (e.g., Komissarov et al. 2007; Palenzuela et al. 2009) have been published. We have chosen a setup similar to that in Palenzuela et al. (2009). It consists of a square covering the range $-6 \leq x \leq 6$, $-0.5 \leq y \leq 0.5$, having a central circular region with a radius $r = \sqrt{x^2 + y^2} \leq 0.8$, where the gas pressure ($p_g = 1$) and the rest-mass density $\rho = 0.01$ are higher than elsewhere ($p_g = \rho = 0.001$; $r > 1$). We note that these values of the thermal pressure and of the rest-mass density are larger than the *standard* ones in RMHD benchmarks, where $p_g = 3 \times 10^{-5}$ and $\rho = 10^{-4}$ for $r > 1$ are adopted. Our RRMHD code is unable to handle such extreme conditions, where the magnetisation of the outer medium is 50 times larger than assumed here, unless a prohibitively small CFL factor or extremely fine grids are employed. The central region is continuously connected with the surroundings using an exponentially decreasing pressure and density in the region $0.8 \leq r \leq 1$. Everywhere in the computational domain, the magnetic field, $\mathbf{B} = (0.1, 0, 0)^T$ ⁵, is uniform, $\mathbf{v} = (0, 0, 0)^T$ and the adiabatic index is $\gamma = 4/3$. The initial data are evolved until $t = 4$. This test is used to validate the new resistive code in 2D and in the ideal limit (a uniform conductivity $\sigma = 10^6$ is set everywhere), in a situation where strong shocks develop (in contrast to the resistive rotor shown in Sect. 5.8).

A direct comparison with an analytic solution is not possible in this case. We note, however, that our results (Fig. 19) compare fairly well with the those obtained with our ideal RMHD code (Leismann et al. 2005; Antón et al. 2010), as well as with the same setup in Palenzuela et al. (2009). As in the latter reference, our solution is also regular everywhere and similar results can be obtained with smaller values of the conductivity, namely with $\sigma \gtrsim 10^4$.

The largest discontinuities in this test are the shocks delimiting the fast expanding shell, whose profiles at $x = 0$ are displayed in Fig. 19 (bottom panels). Thus, resolving the contact waves does not play a major role in the overall dynamics. As a result, the advantage of using the HLLC solver with respect to employing the HLL solver is significantly decreased. Indeed, for this test, the HLLC and HLL solutions basically overlap independently of the spatial reconstruction employed. This fact is evident in Fig. 19 (bottom panels). The solutions computed without any spatial reconstruction are nearly coincident, with tiny discrepancies in the pressure on the central evacuated area of the domain (see yellow and green lines in Fig. 19 bottom panels). Employing a 2nd-order MC reconstruction the HLL and HLLC solutions are almost indistinguishable.

The CE tests performed with the HLLC solver require $\sim 18\%$ larger computational time than those computed with the HLL solver, i.e., in this 2D test the computational overhead of using the HLLC solver is a bit larger than for the RR test. However, looking at the variations of the overheads displayed in Tab. 2, we may conclude that the computational time needed by the HLLC solver is $\sim 5 - 20\%$ larger than

⁵ Palenzuela et al. (2009) employ a weaker magnetic field $\mathbf{B} = (0.05, 0, 0)^T$ in this test.

with the HLL solver, independently of the dimensionality of the problem.

6 ASTROPHYSICAL APPLICATIONS: RELATIVISTIC IDEAL TEARING MODES

The purpose of this section is twofold. On the one hand, we present an astrophysically relevant application of the newly developed numerical method and, on the other hand, we aim to calibrate the ability of the HLLC and HLL solvers to properly obtain the growth rate of relativistic ideal TMs.

The TM instability is a resistive MHD instability that can develop in current sheets and dissipates magnetic energy into kinetic energy and subsequently into thermal energy. TMs disconnect and rejoin magnetic field lines, thereby changing the topology of the magnetic field. The linear theory of TMs was extensively studied, in the context of plasma fusion physics, in a seminal paper of Furth et al. (1963). TMs are of great relevance in astrophysics, (e.g. in the magnetopause or magnetotail of the solar wind, in flares or coronal loops of the Sun, and in the flares of the Crab pulsar; cf. Priest & Forbes 2000). They have been also suggested to be a terminating agent of the MRI (Balbus & Hawley 1991; Latter et al. 2009; Pessah 2010, but see Rembiasz et al. 2016b who observed an MRI termination by the Kelvin-Helmholtz instability in their 3D MRI simulations).

Following Del Zanna et al. (2016), we simulate a relativistic ideal TM in a 2D domain of $[-20a, 20a] \times [0, L_y]$, where $a = 0.01L$, $L_y = 2\pi/k$, and we further set $L = 1$ and $k = 12$. The term *ideal* TM was introduced by Pucci & Velli (2014) who pointed out that current sheets with a thickness $a = S^{-1/3}L$ (where S is the Lunquist number defined below) are unstable agains a TM growing on an Alfvén (*ideal*) timescale in classical resistive MHD. Landi et al. (2015) confirmed that numerically with 2D compressible classical MHD simulations. We use copying and periodic boundary conditions in the directions x and y , respectively, for all variables but B_x . The boundary values of the latter variable in the x direction are computed from the solenoidal constraint $\nabla \cdot \mathbf{B} = 0$. To trigger the TM instability, we perturb the initial background magnetic field

$$B_{0y} = B_0 \tanh(x/a), \quad (51)$$

$$B_{0z} = B_0 \operatorname{sech}(x/a), \quad (52)$$

with

$$B_{1x} = \epsilon B_0 \cos(ky) \operatorname{sech}(x/a), \quad (53)$$

$$B_{1y} = \epsilon k^{-1} B_0 \sin(ky) \tanh(x/a) \operatorname{sech}(x/a). \quad (54)$$

We set $B_0 = \rho_0 = 1$, $p_0 = 0.5$, $\sigma = 2 \times 10^6$, and $\epsilon = 10^{-4}$, so that the magnetisation is $\sigma_m = B_0^2/\rho_0 = 1$, the ratio of magnetic-to-thermal pressure becomes $\beta_0 = B_0^2/(2p_0) = 1$, and the resulting Alfvén speed and Lunquist number are $c_A = 0.5$ and $S \equiv Lc_A\sigma = 10^6$, respectively. For this Lunquist number, Del Zanna et al. (2016) used a resolution of 2048×512 zones. This choice was driven by the fact that for the default resolution chosen by those authors (1024×512), numerical resistivity was higher than the physical one and strongly affected their simulation results. However, in our studies, we used much more moderate resolutions of 512×32 and 1024×32 zones for the following reasons.

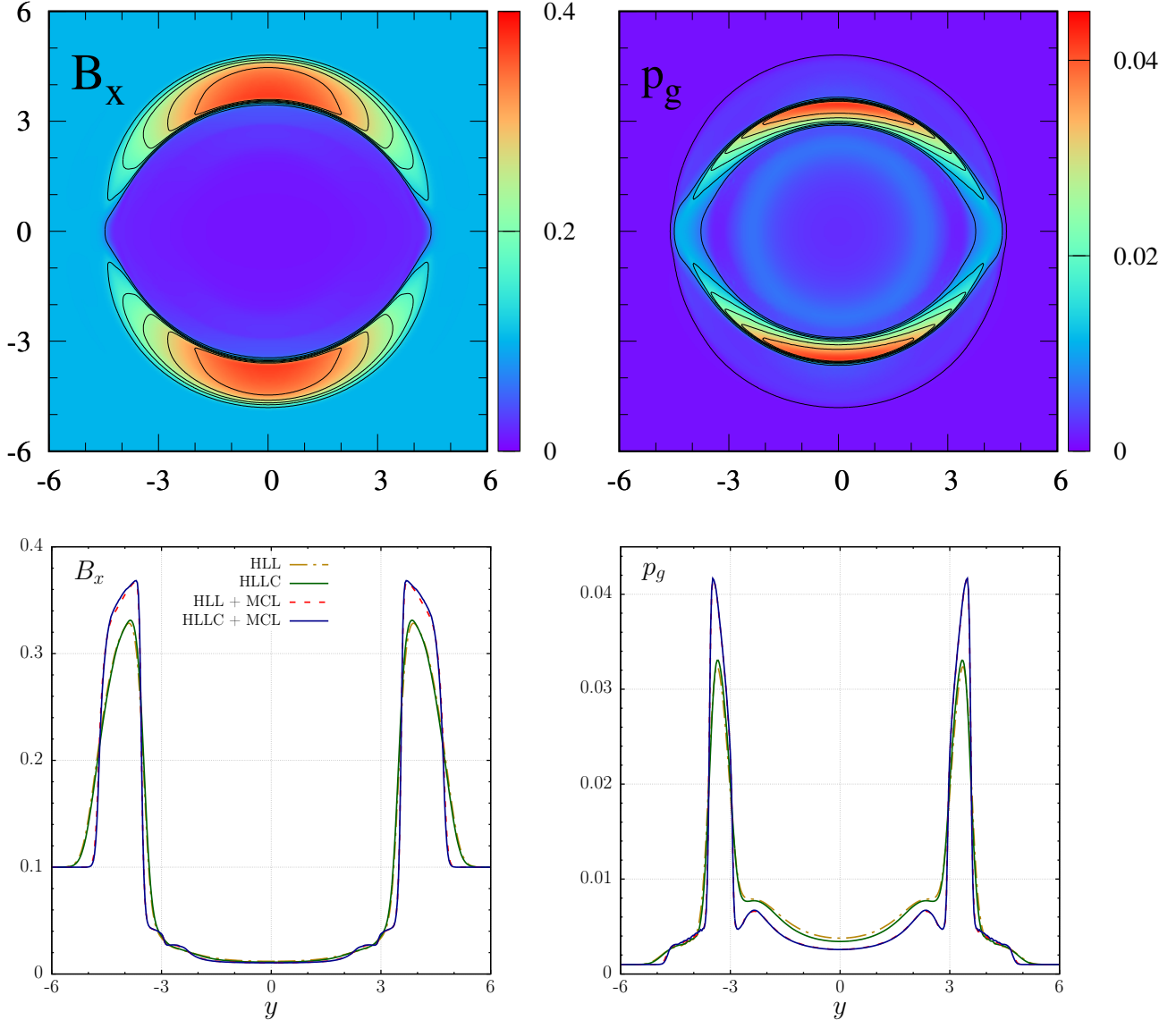


Figure 19. Upper panel: snapshots at $t = 4$, of the magnetic field (B_x component; left) and thermal pressure p_g (right), for the CE test computed with a uniform grid of 400×400 cells, CFL factor $C_{\text{CFL}} = 0.1$, employing the IMEX-RK scheme SSP2(332)-LUM and a MCL intercell reconstruction. Lower panel: profiles along $x = 0$, for B_x (left) and p_g (right). Dash-dotted orange and solid green lines show the 1st-order HLL and HLLC schemes, respectively. Dashed red and solid blue lines show the second order case using the MC spatial reconstruction in combination with the HLL and the HLLC solvers, respectively.

First, because we employ an ultra high-order spatial reconstruction scheme of the 9th-order (MP9; Suresh & Huynh 1997) whose numerical dissipation is much lower than that of other lower order schemes (see the extensive studies of Rembiasz et al. 2017). Second, as we are only interested in the linear phase of the TM instability, we can use a much lower resolution in the y -direction where all perturbed quantities exhibit a (co-)sinusoidal variation. Hence, the characteristic length of the system (Rembiasz et al. 2017) in this direction is equal to the box length, L_y , and it can be very well resolved with 32 zones using the MP9 scheme.

A possible tracer for the growth of the TM instability is the induced growth of the magnetic field component B_x , which after the initial transient phase is assumed to grow as $B_x(t) = B_{1x} e^{\gamma_{\text{TM}} t}$, where B_{1x} is a time independent eigenfunction of the TM. In order to have a positively defined

global quantity we compute the integrated value on the whole computational domain of B_x^2 , i.e., $\mathcal{B} := \int B_x^2(t) \, dS$. Then, we take the logarithm of \mathcal{B} ,

$$\ln \mathcal{B} = 2\gamma_{\text{TM}} t + \ln \left(\int B_{1x}^2 \, dS \right), \quad (55)$$

and obtain γ_{TM} from the slope of the linear fit $\ln \mathcal{B}$ vs t ⁶ in the time interval $t \in [4, 10]$.

Our simulation results (Fig. 20 and Tab. 3) are very similar to those obtained by Del Zanna et al. (2016) (Figs. 1, 3 and 4, therein). The TM instability sets in after $t \approx 2$ and its growth rate (bottom right panel of Fig. 20) is close to

⁶ We note that Del Zanna et al. (2016) employs a different variable to compute γ_{TM} , namely $\ln(\max(B_x))$.

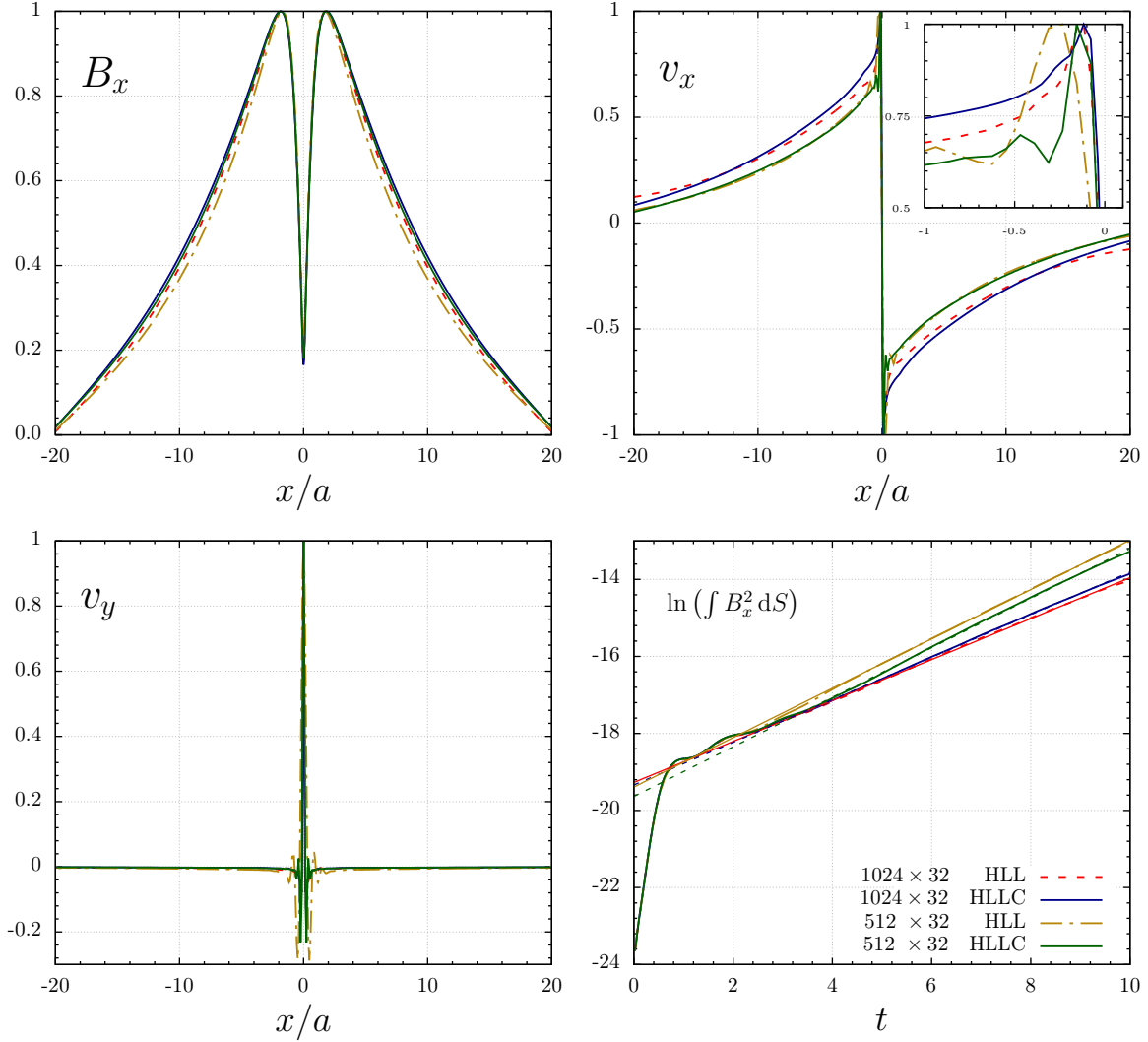


Figure 20. 2D simulations of TMs performed with the HLL and HLLC Riemann solvers, MP9 reconstruction scheme and resolution of 512×32 and 1024×32 zones. All quantities (but in bottom right panel) are presented at $t = 10$ and normalised for a better comparison. *Upper left:* x -component of magnetic field (B_x) at $y = 0$. *Upper right:* x -component of velocity (v_x) at $y = 3L_y/4$. *Bottom left:* y -component of velocity (v_y) at $y = 0$. *Bottom right:* Time evolution of $\ln(\int B_x^2 dS)$. The TM growth rate is determined from a linear fit (solid and dashed lines of the corresponding colours for the HLL and HLLC solvers, respectively) to this quantity for $t \in [4, 10]$ (see Tab. 3).

Table 3. TM growth rate determined from a linear fit of $\ln \mathcal{B}$ (Eq. 55) in the time interval $t \in [4, 10]$ (see bottom right panel of Fig. 20) in simulations performed with the HLLC (second column) and HLL (third column) approximate Riemann solvers and the MP9 spatial reconstruction scheme.

Growth rate		
resolution	HLLC	HLL
512×32	0.322	0.321
1024×32	0.276	0.265

$\gamma_{\text{TM}} = 0.3$, which [Del Zanna et al. \(2016\)](#) obtained both analytically as well as with their numerical code for solving the linearised MHD equations. In simulations performed with the lower resolution, i.e., of 512×32 zones, employing both Riemann solvers, the TM growth-rate is very similar but higher than theoretically expected, i.e., $\gamma_{\text{TM}} \approx 0.32$. We at-

tribute this discrepancy to numerical resistivity. In the simulations performed with 1024×32 zones, the TM growth-rate is lower than theoretically expected, i.e. $\gamma_{\text{TM}} \approx 0.27$. This can be explained by the resistive dissipation of the background magnetic field (as pointed out by [Del Zanna et al. 2016](#), who obtained the same value) as well as by numer-

ical viscosity present in the simulations, since viscosity is known to reduce the TM growth rate (Furth et al. 1963; Rembiasz et al. 2017). The x -components of the magnetic field (B_x) (see the upper left panel of Fig. 20) are similar in all four simulations, however, there are visible differences in the x - and y -components of the velocity. In the simulation performed with the HLL solver and the resolution of 512×32 zones, the (characteristic for the TM instability) velocity peaks of the v_x component (Fig. 20, upper right panel) are located farther away from $x = 0$ than in the other simulations. We attribute this difference to a higher numerical viscosity (and resistivity) of the HLL solver, as the distance between these peaks is proportional to certain (not necessarily equal) powers of viscosity and resistivity (see Rembiasz et al. 2017, for a detailed discussion for a different TM setup). However, it is not necessary invoking the differences in numerical resistivity and viscosity (whose accurate knowledge requires a very careful calibration of the numerical method) between the two solvers employed to assess the superiority of the HLLC solver. Instead, we may compare solutions computed at the two different resolutions used in these series of tests. Looking at the profiles of both v_x and v_y , their resemblance in the case of models run with the HLLC solver is greater than when using the HLL solver. Since the higher resolution models are closer to the actual solution of the problem, this means that tests conducted with the HLLC solver are closer to a converged state than the same models run with the HLL solver.

7 CONCLUSIONS

We have developed a new HLLC approximate Riemann solver for the augmented RRMHD system of equations. The extra equations of the system are used to control the violation of the solenoidal magnetic field constraint and enforce charge conservation to truncation error. The new solver captures exactly isolated stationary contact discontinuities, improving on the single state HLL solver, which in RRMHD reduces to a Local-Lax-Friedrich (global scheme). The new HLLC solver does not need to distinguish between the cases in which the magnetic field perpendicular to a discontinuity is zero or not and thus it does not suffer from any pathological singularity when the component of magnetic field normal to a zone interface approaches zero. Several test problems in 1D and 2D show that the HLLC scheme always displays smaller numerical diffusion than the HLL approximate Riemann solver. The computational overhead with respect to the simpler HLL solver is very modest and its implementation in existing RRMHD codes is straightforward.

The new solver has shown its capability to resolve strong shocks in 2D tests and a good behaviour in different conductivity regimes. For most of the numerical experiments considered, the results are insensitive to the exact value of the conductivity when $\sigma \gtrsim 10^6$. We take this as an indication of the fact that the intrinsic numerical resistivity of our algorithm is $\lesssim 10^{-6}$. Also, this result justifies our choice of a default conductivity ($\sigma = 10^6$) to address the ideal RMHD regime in most of the numerical benchmarks we have conducted.

We find that the models run with the HLLC solver are $\sim 5\% - 20\%$ more computationally expensive than the cor-

responding counterparts employing the HLL solver (Tab. 2). This results hold for both 1D and 2D simulations. The variations in the computational time are closely related to the different number of iterations necessary to solve numerically the quadratic equation (Eq. 45). In view of the fact that the L1-norm errors are systematically smaller employing the HLLC solver than the HLL solver, and also considering the small computational overhead that the HLLC solver introduces, we conclude that the new HLLC solver is a viable alternative to the very broadly used HLL solver.

In our applications with more astrophysical interest, the HLLC Riemann solver also proved to be superior to the HLL solver in 2D simulations of the TM instability. The combination of high-order spatial reconstruction and the HLLC solver helps to accurately estimate the growth rate of the TM instability. We plan to exploit this fact to explore in greater detail the physics of relativistic TMs in the future.

ACKNOWLEDGEMENTS

We acknowledge support from the European Research Council (grant CAMAP-259276) as well as from grants AYA2015-66899-C2-1-P and PROMETEOII/2014-069. S. M-A. acknowledges financial support from COLCIENCIAS conv. 679. The computations have been performed at the Servei d'Informàtica of the University of Valencia. We also thank the anonymous referee whose valuable comments and suggestions allowed us to improve the quality of this manuscript.

APPENDIX A: ALTERNATIVE HLLC SOLVERS

Here, we explore alternatives to the assumption made in Sec. 4 (Eq. 38) on the continuity of the electromagnetic variables. For that, we may generalise the approach of Mignone & Tzeferacos (2010) for RRMHD in combination with the GLM method. When solving a one dimensional Riemann problem at a zone interface (e.g., in the x -direction as we are assuming), the following 2×2 linear hyperbolic sub-systems arise:

$$\begin{cases} \partial_t B_x = -\partial_x \phi, \\ \partial_t \phi = -\partial_x B_x, \end{cases} \quad (A1)$$

$$\begin{cases} \partial_t E_x = -\partial_x \psi, \\ \partial_t \psi = -\partial_x E_x, \end{cases} \quad (A2)$$

$$\begin{cases} \partial_t B_y = +\partial_x E_z, \\ \partial_t E_z = +\partial_x B_y, \end{cases} \quad (A3)$$

$$\begin{cases} \partial_t B_z = -\partial_x E_y, \\ \partial_t E_y = -\partial_x B_z. \end{cases} \quad (A4)$$

We note that in the systems (A3) and (A4) the electric current and the source terms for the GLM scalar potentials are not included since they are treated implicitly by our time integration schemes (either MIRK or RKIMEX). For generic pairs of left and right states $(B_{x,l}, \phi_l)$, $(B_{x,r}, \phi_r)$; $(E_{x,l}, \psi_l)$, $(E_{x,r}, \psi_r)$; $(B_{y,l}, E_{z,l})$, $(B_{y,r}, E_{z,r})$,

and $(B_{z,l}, E_{y,l})$, $(B_{z,r}, E_{y,r})$, the Godunov flux of the systems (A1)-(A4) can be exactly computed as

$$\begin{cases} \hat{B}_x = \frac{B_{x,l} + B_{x,r} - (\phi_r - \phi_l)}{2}, \\ \hat{\phi} = \frac{\phi_{x,l} + \phi_{x,r} - (B_{x,r} - B_{x,l})}{2}, \end{cases} \quad (\text{A5})$$

$$\begin{cases} \hat{E}_x = \frac{E_{x,l} + E_{x,r} - (\psi_r - \psi_l)}{2}, \\ \hat{\psi} = \frac{\psi_{x,l} + \psi_{x,r} - (E_{x,r} - E_{x,l})}{2}, \end{cases} \quad (\text{A6})$$

$$\begin{cases} \hat{B}_y = \frac{B_{y,l} + B_{y,r} + (E_{z,r} - E_{z,l})}{2}, \\ \hat{E}_z = \frac{E_{z,l} + E_{z,r} + (B_{y,r} - B_{y,l})}{2}, \end{cases} \quad (\text{A7})$$

$$\begin{cases} \hat{B}_z = \frac{B_{z,l} + B_{z,r} - (E_{y,r} - E_{y,l})}{2}, \\ \hat{E}_y = \frac{E_{y,l} + E_{y,r} - (B_{z,r} - B_{z,l})}{2}. \end{cases} \quad (\text{A8})$$

Therefore, we may obtain the solution of the 2×2 linear Riemann problems separately before using a standard Riemann solver for the remaining set of one-dimensional equations. The electric and magnetic field components as well as the scalar potentials ϕ and ψ precomputed with Eqs. (A5)-(A8) enter as constant parameters in the computation of the numerical Riemann fluxes. Our choice is to employ an HLLC approximate Riemann solver built as in Sec. 4. In this case, the only numerical fluxes that need to be computed are the ones corresponding to $(q, D^*, S_x^*, S_y^*, S_z^*, \mathcal{E}^*)$.

We note that the numerical fluxes of the conserved variables $(\phi, \psi, B_x, B_y, B_z, E_x, E_y, E_z)$ corresponding to the exact solutions written in Eqs. (A5)-(A8) are $(\hat{B}_x, \hat{E}_x, \hat{\phi}, -\hat{E}_z, \hat{E}_y, \hat{\psi}, \hat{B}_z, -\hat{B}_y)$, respectively. It turns out that the expressions for these fluxes coincide with those that we obtain in the HLLC solver described in the Sec. 4 (Eq. 39) if we fix $\lambda_l = -1$ and $\lambda_r = +1$. Remarkably, the numerical fluxes of Eq. (39) result from the assumption that the conserved variables $(\phi, \psi, B_x, B_y, B_z, E_x, E_y, E_z)$ are continuous across the contact wave. Therefore, we do not expect that precomputing the exact solutions given in (A5)-(A8) and then using them as parameters in the rest of the HLLC solver may bring any improvement in the numerical solution of the RRMHD equations in comparison with employing the full HLLC solver as presented in in Sec. 4 with $\lambda_l = -1$ and $\lambda_r = +1$. Nonetheless, the usage of Eqs. (A5)-(A8) as parameters for the rest of the solver may yield a reduced numerical viscosity of the algorithm. The reason is that we are not necessarily bound to use values $\lambda_l = -1$ and $\lambda_r = +1$ as the limiting speeds for the variables $(q, D^*, S_x^*, S_y^*, S_z^*, \mathcal{E}^*)$. For this reduced set of conserved variables, the eigenvalues of the corresponding Jacobian matrix are $\lambda_q = \lambda_{H_0} = v_x$ and $\lambda_{H_{\pm}}$ (Eqs. 16-18), and the maximum and minimum signal speeds can be taken as

$$\begin{aligned} \lambda_l &= \min \{ \lambda_{H_{-l}}, \lambda_{H_{-r}} \}, \\ \lambda_r &= \max \{ \lambda_{H_{+l}}, \lambda_{H_{+r}} \}. \end{aligned} \quad (\text{A9})$$

We have tested this *hybrid* HLLC solver with all the 1D and 2D tests presented in Sections 5 and 6 and found that it basically provides the same quantitative results as the solver delineated in Sec. 4. Nevertheless, this alternative solver introduces less numerical viscosity, which manifests itself in small oscillations arising close to discontinuities in 2D tests,

making it a bit less robust to, e.g. accurately predict the growth rate of relativistic TMs.

REFERENCES

Abgrall R., Karni S., 2001, *Journal of Computational Physics*, **169**, 594
 Acciari V. A., et al., 2008, *ApJ*, **679**, 397
 Aharonian F., et al., 2006, *Science*, **314**, 1424
 Aharonian F., et al., 2007, *ApJ*, **664**, L71
 Akiyama S., Wheeler J. C., Meier D. L., Lichtenstadt I., 2003, *ApJ*, **584**, 954
 Albert J., et al., 2007, *ApJ*, **669**, 862
 Albert J., et al., 2008, *ApJ*, **685**, L23
 Aloy M. Á., Cordero-Carrión I., 2016, *Journal of Physics: Conference Series*, **719**, 012015
 Aloy M. A., Ibáñez J. M., Martí J. M., Müller E., 1999, *ApJS*, **122**, 151
 Anile A. M., 1989, *Relativistic fluids and magneto-fluids: with applications in astrophysics and plasma physics*. Cambridge University Press
 Antón L., Miralles J. A., Martí J. M., Ibáñez J. M., Aloy M. A., Mimica P., 2010, *ApJS*, **188**, 1
 Balbus S. A., Hawley J. F., 1991, *ApJ*, **376**, 214
 Balbus S. A., Hawley J. F., 1998, *Reviews of Modern Physics*, **70**, 1
 Balsara D., 2001, *The Astrophysical Journal Supplement*, **132**, 83
 Barniol Duran R., Leng M., Giannios D., 2016, *MNRAS*, **455**, L6
 Begelman M. C., 1998, *ApJ*, **493**, 291
 Beloborodov A. M., 2013a, *ApJ*, **762**, 13
 Beloborodov A. M., 2013b, *ApJ*, **777**, 114
 Beloborodov A. M., Thompson C., 2007, *ApJ*, **657**, 967
 Beskin V. S., Kuznetsova I. V., 2000, *Nuovo Cimento B Serie*, **115**, 795
 Bicknell G. V., Wagner S. J., 2002, *Publ. Astron. Soc. Australia*, **19**, 129
 Blandford R. D., 2002, in Gilfanov M., Sunyeav R., Churazov E., eds, *Lighthouses of the Universe: The Most Luminous Celestial Objects and Their Use for Cosmology*. p. 381 ([arXiv:astro-ph/0202265](https://arxiv.org/abs/astro-ph/0202265)), doi:10.1007/10856495_59
 Blandford R. D., Znajek R. L., 1977, *MNRAS*, **179**, 433
 Brio M., Wu C. C., 1988, *J. Comp. Phys.*, **75**, 400
 Bromberg O., Tchekhovskoy A., 2016, *MNRAS*, **456**, 1739
 Bucciantini N., Del Zanna L., 2013, *MNRAS*, **428**, 71
 Bucciantini N., Del Zanna L., Amato E., Volpi D., 2005, *A&A*, **443**, 519
 Cerdá-Durán P., Font J. A., Dimmelmeier H., 2007, *A&A*, **474**, 169
 Chandrasekhar S., 1960, *Proc. of the Nat. Acad. of Science*, **46**, 253
 Chen G.-Q., Levermore C. D., Liu T.-P., 1994, *Communications on Pure and Applied Mathematics*, **47**, 787
 Contopoulos I., Kazanas D., Papadopoulos D. B., 2013, *ApJ*, **765**, 113
 Cordero-Carrión I., Ibáñez J. M., Aloy M. Á., 2012, in Beltrán Jiménez J., Ruiz Cembranos J. A., Dobado A., López Maroto A., De la Cruz Dombriz A., eds, Vol. 1458, American Institute of Physics Conference Series. pp 359–362, doi:10.1063/1.4734434
 Daigne F., Mochkovitch R., 2002, *MNRAS*, **336**, 1271
 Dedner A., Kemm F., Kröner D., Munz C.-D., Schnitzer T., Weisenberg M., 2002, *J. Comp. Phys.*, **175**, 645
 Del Zanna L., Bucciantini N., Londrillo P., 2003, *A&A*, **400**, 397
 Del Zanna L., Papini E., Landi S., Bugli M., Bucciantini N., 2016, *MNRAS*, **460**, 3753
 Deng W., Li H., Zhang B., Li S., 2015, *ApJ*, **805**, 163

Dixon W. G., 1978, Special relativity: the foundation of macroscopic physics.. Cambridge Univ. Press

Dumbser M., Zanotti O., 2009, *J. Comp. Phys.*, **228**, 6991

Eichler D., 1993, *ApJ*, **419**, 111

Evans C. R., Hawley J. F., 1988, *ApJ*, **332**, 659

Fernández R., Metzger B. D., 2016, *Annual Review of Nuclear and Particle Science*, **66**, 23

Forth H. P., Killeen J., Rosenbluth M. N., 1963, *Physics of Fluids*, **6**, 459

Ghosh P., 2000, *MNRAS*, **315**, 89

Giacomazzo B., Rezzolla L., 2006, *Journal of Fluid Mechanics*, **562**, 223

Giannios D., 2013, *MNRAS*, **431**, 355

Giannios D., Spruit H. C., 2005, *A&A*, **430**, 1

Giannios D., Spruit H. C., 2006, *A&A*, **450**, 887

Giannios D., Uzdensky D. A., Begelman M. C., 2009, *MNRAS*, **395**, L29

Giannios D., Uzdensky D. A., Begelman M. C., 2010, *MNRAS*, **402**, 1649

Goodman J., Uzdensky D., 2008, *ApJ*, **688**, 555

Goodman J., Xu G., 1994, *ApJ*, **432**, 213

Guilet J., Müller E., 2015, *MNRAS*, **450**, 2153

Guilet J., Müller E., Janka H.-T., 2015, *MNRAS*, **447**, 3992

Gurski K. F., 2004, *SIAM Journal on Scientific Computing*, **25**, 2165

Harten A., Lax P. D., van Leer B., 1983, *SIAM Review*, **25**, 35

Hesse M., Zenitani S., 2007, *Physics of Plasmas*, **14**, 112102

Honkkila V., Janhunen P., 2007, *Journal of Computational Physics*, **223**, 643

Kim J., Balsara D. S., 2014, *Journal of Computational Physics*, **270**, 634

Komissarov S. S., 1999, *MNRAS*, **303**, 343

Komissarov S. S., 2004, *MNRAS*, **350**, 427

Komissarov S. S., 2007, *MNRAS*, **382**, 995

Komissarov S. S., Barkov M., Lyutikov M., 2007, *MNRAS*, **374**, 415

Kumar P., 1999, *ApJ*, **523**, L113

Kumar P., Narayan R., 2009, *MNRAS*, **395**, 472

Landi S., Del Zanna L., Papini E., Pucci F., Velli M., 2015, *ApJ*, **806**, 131

Latter H. N., Lesaffre P., Balbus S. A., 2009, *MNRAS*, **394**, 715

Lazar A., Nakar E., Piran T., 2009, *ApJ*, **695**, L10

LeVeque R. J., 2002, Finite volume methods for hyperbolic problems. Cambridge texts in applied mathematics, Cambridge University Press, Cambridge, New York, <http://opac.inria.fr/record=b1100566>

Leismann T., Antón L., Aloy M. A., Müller E., Martí J. M., Miralles J. A., Ibáñez J. M., 2005, *Astronomy and Astrophysics*, **436**, 503

Levinson A., Segev N., 2017, preprint, ([arXiv:1709.09397](https://arxiv.org/abs/1709.09397))

Li S., 2005, *J. Comp. Phys.*, **203**, 344

Lyubarsky Y. E., 2005, *MNRAS*, **358**, 113

Lyutikov M., 2006, *MNRAS*, **369**, L5

Lyutikov M., Blandford R., 2003, ArXiv Astrophysics e-prints,

Marrone D. P., Moran J. M., Zhao J.-H., Rao R., 2007, *ApJ*, **654**, L57

Marscher A. P., Gear W. K., 1985, *ApJ*, **298**, 114

Martí J.-M., 2015, *Computer Physics Communications*, **191**, 100

Martí J. M., Müller E., 2015, *Living Reviews in Computational Astrophysics*, **1**, 3

Martí-Vidal I., Muller S., Vlemmings W., Horellou C., Aalto S., 2015, *Science*, **348**, 311

McKinney J. C., 2006, *MNRAS*, **367**, 1797

McKinney J. C., Gammie C. F., 2004, *ApJ*, **611**, 977

McKinney J. C., Uzdensky D. A., 2012, *MNRAS*, **419**, 573

Meier D. L., 2003, *New Astron. Rev.*, **47**, 667

Mignone A., Bodo G., 2005, *MNRAS*, **364**, 126

Mignone A., Bodo G., 2006, *MNRAS*, **368**, 1040

Mignone A., Tzeferacos P., 2010, *J. Comp. Phys.*, **229**, 2117

Mignone A., Ugliano M., Bodo G., 2009, *MNRAS*, **393**, 1141

Mimica P., Aloy M. A., 2010, *MNRAS*, **401**, 525

Mimica P., Aloy M. A., Müller E., Brinkmann W., 2004, *A&A*, **418**, 947

Mimica P., Aloy M. A., Müller E., Brinkmann W., 2005, *A&A*, **441**, 103

Mimica P., Aloy M. A., Müller E., 2007, *A&A*, **466**, 93

Miranda-Aranguren S., Aloy M. A., Aloy-Torás C., 2014, in Pogorelov N. V., Audit E., Zank G. P., eds, Astronomical Society of the Pacific Conference Series Vol. 488, 8th International Conference of Numerical Modeling of Space Plasma Flows (ASTRONUM 2013). p. 249

Mizuno Y., 2013, *ApJS*, **205**, 7

Mohseni F., Mendoza M., Succi S., Herrmann H. J., 2015, *Phys. Rev. E*, **92**, 023309

Mösta P., Ott C. D., Radice D., Roberts L. F., Schnetter E., Haas R., 2015, *Nature*, **528**, 376

Mouschovias T. C., Paleologou E. V., 1980, *ApJ*, **237**, 877

Nalewajko K., Giannios D., Begelman M. C., Uzdensky D. A., Sikora M., 2011, *MNRAS*, **413**, 333

Narayan R., Kumar P., 2009, *MNRAS*, **394**, L117

Narayan R., Piran T., 2012, *MNRAS*, **420**, 604

Nathanail A., Contopoulos I., 2014, *ApJ*, **788**, 186

Noh W. F., 1987, *Journal of Computational Physics*, **72**, 78

O'Riordan M., Pe'er A., McKinney J. C., 2017, *ApJ*, **843**, 81

Obergaulinger M., Aloy M. Á., 2017, *MNRAS*, **469**, L43

Obergaulinger M., Aloy M. A., Dimmelmeier H., Müller E., 2006, *A&A*, **457**, 209

Okamoto I., 2006, *PASJ*, **58**, 1047

Palenzuela C., Lehner L., Reula O., Rezzolla L., 2009, *MNRAS*, **394**, 1727

Palenzuela C., Lehner L., Liebling S. L., 2010, *Science*, **329**, 927

Panaiteescu A., Spada M., Mészáros P., 1999, *ApJ*, **522**, L105

Pareschi L., Russo G., 2005, *Journal of Scientific Computing*, **25**, 129

Parfrey K., Giannios D., Beloborodov A. M., 2015, *MNRAS*, **446**, L61

Pember R. B., 1993, *SIAM Journal on Scientific Computing*, **14**, 824

Penna R. F., Narayan R., Sadowski A., 2013, *MNRAS*, **436**, 3741

Pessah M. E., 2010, *ApJ*, **716**, 1012

Petropoulou M., Giannios D., Sironi L., 2016, *MNRAS*, **462**, 3325

Petschek H. E., 1964, NASA Special Publication, **50**, 425

Pons J. A., Font J. A., Ibanez J. M., Martí J. M., Miralles J. A., 1998, *A&A*, **339**, 638

Priest E., Forbes T., 2000, Magnetic Reconnection. Cambridge University Press

Pucci F., Velli M., 2014, *ApJ*, **780**, L19

Qian Q., Fendt C., Noble S., Bugli M., 2017, *ApJ*, **834**, 29

Rees M. J., 1978, *MNRAS*, **184**, 61P

Rees M. J., Mészáros P., 1994, *ApJ*, **430**, L93

Rembiasz T., Obergaulinger M., Cerdá-Durán P., Müller E., Aloy M. A., 2016a, *MNRAS*, **456**, 3782

Rembiasz T., Guilet J., Obergaulinger M., Cerdá-Durán P., Aloy M. A., Müller E., 2016b, *MNRAS*, **460**, 3316

Rembiasz T., Obergaulinger M., Cerdá-Durán P., Aloy M.-Á., Müller E., 2017, *ApJS*, **230**, 18

Rezzolla L., Giacomazzo B., Baiotti L., Granot J., Kouveliotou C., Aloy M. A., 2011, *ApJ*, **732**, L6

Sawai H., Yamada S., 2016, *ApJ*, **817**, 153

Sawai H., Yamada S., Suzuki H., 2013, *ApJ*, **770**, L19

Sironi L., Petropoulou M., Giannios D., 2015, *MNRAS*, **450**, 183

Spada M., Ghisellini G., Lazzati D., Celotti A., 2001, *MNRAS*, **325**, 1559

Spruit H. C., Daigne F., Drenkhahn G., 2001, *A&A*, **369**, 694

Stone J. M., Norman M. L., 1992, *ApJS*, **80**, 791

Suresh A., Huynh H. T., 1997, *Journal of Computational Physics*, **136**, 83

Takamoto M., 2013, *ApJ*, **775**, 50

Takamoto M., 2014, in Pogorelov N. V., Audit E., Zank G. P., eds, *Astronomical Society of the Pacific Conference Series Vol. 488, 8th International Conference of Numerical Modeling of Space Plasma Flows (ASTRONUM 2013)*. p. 267

Takamoto M., Inoue T., 2011, *ApJ*, **735**, 113

Tchekhovskoy A., Narayan R., McKinney J. C., 2010, *ApJ*, **711**, 50

Tenbarge J. M., Hazeltine R. D., Mahajan S. M., 2010, *MNRAS*, **403**, 335

Thompson C., 1994, *MNRAS*, **270**, 480

Toro E. F., 1997, *Splitting Schemes for PDEs with Source Terms*. Springer Berlin Heidelberg, pp 497–507, doi:10.1007/978-3-662-03490-3_15, https://doi.org/10.1007/978-3-662-03490-3_15

Toro E. F., Spruce M., Speares W., 1994, *Shock Waves*, **4**, 25

Uzdensky D. A., 2011, *Space Sci. Rev.*, **160**, 45

Varnière P., Rodriguez J., Tagger M., 2002, *A&A*, **387**, 497

Velikhov E. P., 1959, *Zh. Eksp. Teor. Fiz.*, **36**, 1398

Vlahakis N., Königl A., 2003, *ApJ*, **596**, 1104

Watanabe N., Yokoyama T., 2006, *ApJ*, **647**, L123

Whitham G. B., 1974, *Linear and nonlinear waves*. John Wiley & Sons, Ltd, New York

Zenitani S., Hesse M., 2008, *ApJ*, **684**, 1477

Zenitani S., Hoshino M., 2007, *ApJ*, **670**, 702

Zenitani S., Hesse M., Klimas A., 2009, *ApJ*, **696**, 1385

Zenitani S., Hesse M., Klimas A., 2010, *ApJ*, **716**, L214

Zhang B., Mészáros P., 2002, *ApJ*, **581**, 1236

Zhang B., Pe'er A., 2009, *ApJ*, **700**, L65

Zhang B., Yan H., 2011, *ApJ*, **726**, 90

This paper has been typeset from a *T_EX/L_AT_EX* file prepared by the author.